

## Automated salt-dome detection using an attribute ranking framework with a dictionary-based classifier

Asjad Amin<sup>1</sup>, Mohamed Deriche<sup>2</sup>, Muhammad Amir Shafiq<sup>3</sup>, Zhen Wang<sup>3</sup>, and Ghassan AlRegib<sup>3</sup>

### Abstract

We have developed a dictionary-based classification approach for salt-dome detection within migrated seismic volumes. The proposed workflow uses seismic attributes derived from the gray-level co-occurrence matrix, Gabor filter, and higher order singular-value decomposition to effectively learn and detect the salt bodies. We use an information theoretic framework to rank the seismic attributes as per their salt-dome classification performance. Based on this ranking, we select the top K attributes for dictionary training, testing, and classification. To improve the accuracy of the detected salt bodies and make the proposed workflow robust to different data sets, we introduce a refining step that uses edge strength and energy values to detect the shape of the salt-dome boundary within the classified patches. The optimal set of attributes and the refining step ensure that the proposed workflow yields good results for detecting salt-dome boundaries even in the presence of weak seismic reflections. We use the seismic data from the Netherlands offshore F3 block (North Sea) to demonstrate the effectiveness of the proposed workflow in detecting salt bodies. Using subjective and objective evaluation metrics, we compare the results of the proposed workflow with existing gradient-, texture-, and patch-based classification methods. The experimental results show that the proposed workflow outperforms existing salt-dome delineation techniques in terms of accuracy and precision.

### Introduction

Salt diapirs are important structures in the earth subsurface; they have excellent sealing capabilities and contain information about major accumulations of petroleum and gas reservoirs. Therefore, determining the accurate location of salt domes within migrated seismic volumes is one of the key steps in exploration projects. However, with the increasing size of seismic volumes, manual interpretation of salt domes is becoming extremely time consuming and labor intensive. To overcome this laborious task, researchers in academia and industry have proposed several fully and semiautomated algorithms for detecting salt bodies within seismic volumes. Over the past few decades, researchers have proposed several edge-based, texture-based, hybrid (edge and texture), normalized cuts, active contour, and patch-based classification methods for salt-dome delineation.

The edge-based detection techniques introduced by Jing et al. (2007), Aqrabi et al. (2011), and Amin and Deriche (2015b) are simple yet effective in detecting the salt-dome boundaries in seismic data. In Jing et al.

(2007) and Aqrabi et al. (2011), a more general form of the Sobel algorithm is implemented by applying masks with different weights and then combining the weighted samples for better delineation. In Amin and Deriche (2015b), a 3D multidirectional edge detector is proposed, which computes the edge map using the 3D Sobel operators in the horizontal, vertical, and diagonal directions. The edge-based detection techniques yield good results when seismic data exhibit strong amplitude variations. However, edge-detection-based segmentation algorithms are very sensitive to the noise present in seismic data. Such schemes often confuse local discontinuities and amplitude variations. In the case of large amplitude variations, these techniques fail to provide a refined salt-dome boundary.

The normalized cuts image segmentation (NCIS) algorithm proposed by Shi and Malik (2000) detects salt domes by solving a global optimization problem. Therefore, it is less sensitive to local discontinuities. Lomask and Biondi (2003) and Lomask et al. (2004, 2006) use the NCIS-based algorithms for detecting salt domes. However, NCIS-based algorithms are computationally very

<sup>1</sup>King Fahd University of Petroleum and Minerals (KFUPM), Center for Energy and Geo Processing (CeGP), Dhahran, Saudi Arabia and the Islamia University of Bahawalpur (IUB), Pakistan. E-mail: asjad.amin@iub.edu.pk

<sup>2</sup>King Fahd University of Petroleum and Minerals (KFUPM), Center for Energy and Geo Processing (CeGP), Dhahran, Saudi Arabia. E-mail: mderiche@kfupm.edu.sa

<sup>3</sup>Georgia Institute of Technology, Atlanta, Georgia, USA. E-mail: amirshafiq@gatech.edu; zwang313@gatech.edu; alregib@gatech.edu.

Manuscript received by the Editor 14 June 2016; revised manuscript received 17 February 2017; published online 26 June 2017. This paper appears in *Interpretation*, Vol. 5, No. 3 (August 2017); p. SJ61–SJ79, 24 FIGS., 8 TABLES.

<http://dx.doi.org/10.1190/INT-2016-0084.1>. © 2017 Society of Exploration Geophysicists and American Association of Petroleum Geologists. All rights reserved.

expensive and limit their applications in seismic interpretation (Lomask et al., 2006).

Salt-boundary segmentation methods introduced by Zhang and Halpert (2012), Hauks et al. (2013), and Shafiq et al. (2015a) are based on active contour models (ACMs), which combine the interpreter's input with automated segmentation. The initial boundary information is provided by a geophysics expert and based on an initial estimate, the ACMs iteratively optimize the cost function to yield a salt-dome boundary. However, providing an initial estimate of the salt dome and designing a cost function are time consuming and require input from an interpreter at each seismic inline section.

Salt boundaries are often characterized by changes in texture rather than reflectivity. Therefore, using only boundary-sensitive attributes such as instantaneous amplitude may degrade the interpretation of salt bodies. Salt-dome detection methods based on texture attributes are proposed by Berthelot et al. (2012, 2013) and Hegazy and AlRegib (2014). The gradient of texture (GoT) method for salt-dome detection, recently introduced by Shafiq et al. (2015b) and Wang et al. (2015), measures the texture dissimilarity between two neighboring cubes and windows, respectively, to detect the salt-dome boundaries. However, the challenge with texture-based schemes is to obtain the most important attributes, which not only represent texture information but are also computationally less expensive.

A hybrid approach based on edge- and texture-based attributes is presented in Amin and Deriche (2015a), and it detects the salt-dome boundary by fusing the output of two classifiers based on the edge and texture attributes at the decision level. The fusion is done at the decision level. The fusion of edge- and texture-based methods can be done at the attributes level, classifier level, or decision level. Therefore, the choice of fusion is important because it affects the overall accuracy of the system.

Patch-based classification methods are widely used in image processing for segmentation, recognition, identification, and classification applications. In Amin et al. (2015), a dictionary-based salt-dome detection method using salt boundary and nonsalt boundary patches is discussed. Although this dictionary-based method detects the salt boundary with good accuracy, it is computationally expensive and requires a solution to an  $l_1$ -minimization problem to classify each patch, which can be problematic.

In this work, we propose a robust dictionary-based learning workflow for salt-dome detection. Despite the substantial literature on dictionary-based classification, segmentation methods based on such models have rarely been used in seismic applications, such as salt-dome detection. We use an optimal feature set obtained from the attributes computed using the gray-level co-occurrence matrix (GLCM), Gabor filter, and higher order singular-value decomposition (HOSVD). The proposed algorithm yields better results using reduced number of features as compared with the other texture

attributes based salt-dome detection methods. The main contributions of this paper include

- a patch-based salt-dome detection method using the dictionary-based classifier
- new attributes extracted from the HOSVD combined with the attributes extracted from the GLCM and Gabor filter
- an information theory-based framework to rank the features based on their relevance and significance
- use of ranked features in dictionary learning and classification
- use of homotopy-based solver for  $\ell_1$ -minimization to increase computational efficiency
- a boundary refining step, based on the edge strength and energy values to overcome the drawbacks of existing patch-based salt-dome detection methods.

The rest of the paper is structured as follows: We present the proposed salt-dome detection algorithm, which includes the formulation of a dictionary-based classifier, the attributes used for learning, and the proposed refining step. Then, we discuss the experiment results and present comparisons with the state of the art.

### The proposed salt-dome detection algorithm

The proposed algorithm works by creating a dictionary from the available training data. The training slices are first partitioned into small patches of size  $N \times N$  samples. Next, we compute the GLCM, Gabor filter, and HOSVD-based features for these patches. These features are then ranked using three information theoretic-based models: (1) the mutual information feature selection (MIFS) criterion, (2) minimum redundancy maximum relevance (mRMR) criterion, and (3) joint mutual information (JMI) criterion. The top ranked features are selected and concatenated to form a dictionary. For a given test slice, the proposed scheme first partitions it into small nonoverlapping patches. By solving an  $\ell_1$ -minimization problem, each patch is classified as either a salt boundary or a non-salt boundary patch. To get an accurate salt boundary from these classified patches, we use a combination of the energy value and edge strength to detect the correct boundary points within each patch. We obtain the outline of the salt boundary by combining all the boundary points. Figure 1 shows the workflow for the proposed algorithm. We will now discuss each of the blocks from Figure 1 in more details.

### Gray-level co-occurrence matrix attributes

The GLCM approximates the joint-probability distribution of two gray levels in an image. The high values away from the diagonal in a GLCM reveal sharp gray-level changes, whereas the high values close to the diagonal reveal small variations in gray levels. The GLCM-based attributes discussed by Haralick et al. (1973) were first applied in Gao (2003) to detect salt boundaries. These attributes can detect the changes in texture among a pair

of pixels along a chosen direction and neighborhood. The joint-probability distribution,  $P_{\text{GLCM}}(i,j)$ , is computed as

$$P_{\text{GLCM}}(i,j) = \frac{q_{d,\theta}(i,j)}{\sum_{i,j} q_{d,\theta}(i,j)}, \quad (1)$$

where  $q_{d,\theta}(i,j)$  represents the number of occurrences of gray levels separated by a distance  $d$  in the direction  $\theta$ . From the  $[P_{\text{GLCM}}]$ , the following attributes are obtained:

#### GLCM entropy

GLCM entropy is a measure of spatial disorder in textures. GLCM entropy is computed as

$$\text{Entropy} = -\sum_i \sum_j P_{\text{GLCM}}(i,j) \log P_{\text{GLCM}}(i,j). \quad (2)$$

Salt areas have a homogeneous texture. GLCM entropy is a measure of spatial disorder in textures. Therefore, the value of this attribute is high along the salt boundaries where the texture is not homogeneous. The value is low for salt areas due to spatial homogeneity inside the salt domes (Berthelot et al., 2013).

#### GLCM energy

GLCM energy is computed as

$$\text{Energy} = \left[ \sum_i \sum_j P_{\text{GLCM}}(i,j)^2 \right]^{\frac{1}{2}}. \quad (3)$$

The dominant edges, due to strong reflections, in a slice give high energy values. Therefore, the value of GLCM energy attribute is high for strong reflectors along the salt boundary (Berthelot et al., 2013).

#### GLCM variance

The GLCM variance measures the gray-level variations of neighboring pairs in an image:

$$\text{Variance} = \sum_i \sum_j |i-j|^2 P_{\text{GLCM}}(i,j). \quad (4)$$

The GLCM variance in an image is low if the neighboring points have similar amplitudes. This feature measures local gray-level variations (or linear dependencies). Salt regions have a homogeneous texture; therefore, the value of the variance is low for these areas. The value of the GLCM variance is high for salt boundaries, which are rich in texture.

In Figure 2, we show the results of GLCM attributes calculated for inline #354 from F3 block. The block covers an area of  $24 \times 16$  km. The inline range is from 100 to 750, the crossline range is 300–1250, the time direction ranges from 0 to 1848 ms sampled at every 4 ms, and the bin size is 25 m in inline and crossline directions.

In Figure 2, we observe that the GLCM attributes extracted from 2D window are not able to detect the weak amplitudes accurately.

#### Gabor filter-based attributes

The periodicity and orientation of seismic textures can be described using attributes derived from the Fourier spectrum. Frequency-based texture attributes are used to extract the impact of reflectors. Gabor filters, as discussed by Randen and Sønneland (2005), can be used in seismic image processing to extract frequency-based attributes. The normalized energy values computed from the Gabor-filtered images were used as the frequency attributes. Different choice of parameters can discriminate between seismic textures with different frequency content. Gabor filters are designed to find the dominant size and orientation of different textures in the image. The Gabor filter with phase  $\phi$  along the  $x$ -axis (orientation =  $0^\circ$ ) and a given radial frequency  $F_R$  is written as

$$h(x,y) = \exp \left\{ -\frac{1}{2} \left[ \frac{x^2}{\sigma_x^2} + \frac{y^2}{\sigma_y^2} \right] \right\} \cos(2\pi F_R x + \phi). \quad (5)$$

For  $\phi = 0$ , the frequency response is given by

$$H(u,v) = \frac{8\sigma_u\sigma_v}{\pi} \left( \exp \left( -\frac{1}{2} \left[ \frac{(u-F_R)^2}{\sigma_u^2} + \frac{v^2}{\sigma_v^2} \right] \right) + \exp \left( -\frac{1}{2} \left[ \frac{(u+F_R)^2}{\sigma_u^2} + \frac{v^2}{\sigma_v^2} \right] \right) \right), \quad (6)$$

where  $u = u \cos \theta + v \sin \theta$ ,  $v = -u \sin \theta + v \cos \theta$ ,  $\theta$  is the orientation, and  $\sigma_u = (1/2\pi\sigma_x)$  and  $\sigma_v = (1/2\pi\sigma_y)$  specify the filter width. For our experiments, and in consistency with previous work (Jain and Farrokhnia, 1991), we have used  $F_R = 2\sqrt{2}$  and  $\sigma_x = \sigma_y = 4$ .

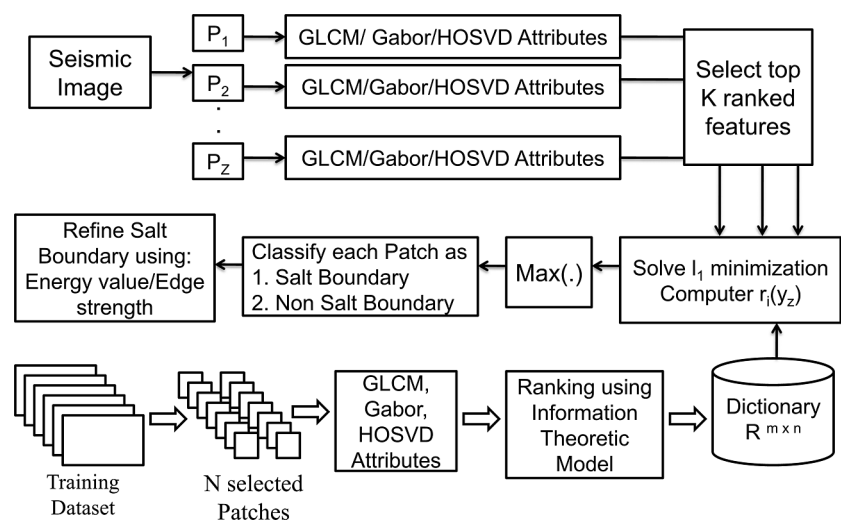


**Figure 1.** The proposed algorithm; bottom row: dictionary training using salt and nonsalt patches, top row: creating feature sets from patches ( $P_i$  =  $i$ th patch) extracted from test inline, and middle row: classification using the trained dictionary.

In Figure 3, we show the result for the Gabor filter-based attribute computed for inline #354. To keep the complexity of the proposed workflow to a minimum, we have used the GLCM and Gabor-filter attributes calculated from 2D patches.

### HOSVD-based attributes

Tensors are multimode or multidimensional arrays. An  $N$ th-order tensor,  $A \in \mathbb{R}^{I_1 \times I_2 \times \dots \times I_N}$ , is a multidimensional array of  $N$  dimensions, where  $I_m$  is the upper

limit of the  $m$ th dimension. In the literature, the order of a tensor is also referred to as mode. A vector is therefore a tensor of first order, a matrix is a tensor of second order, and a 3D volume is a tensor of third order. The 3D seismic data,  $S \in \mathbb{R}^{I \times J \times K}$ , can be considered as a tensor of third order (see Figure 4), where  $I$ ,  $J$ , and  $K$  are the upper limits of each dimension.

For simplicity, tensors can be decomposed into subtensors: fibers (1D) or slices (2D). Fibers are column vectors defined by fixing every index of higher order

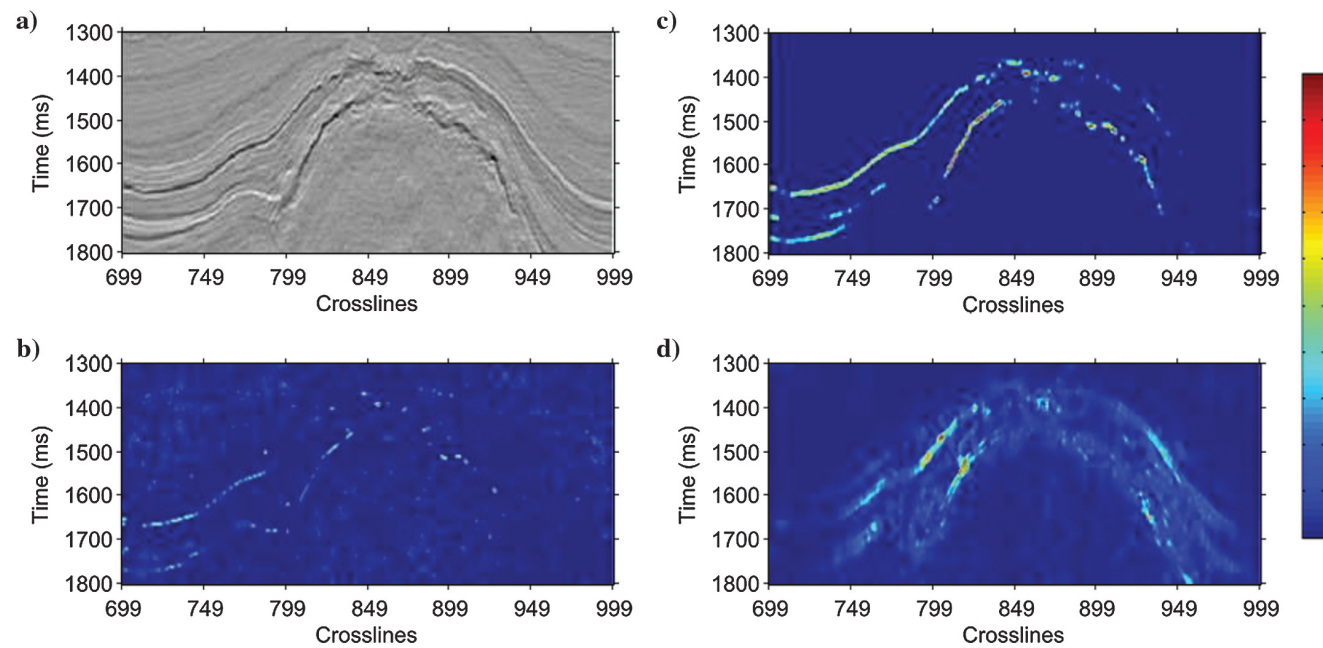


**Figure 2.** (a) Inline #354 (F3 block), and (b-d) GLCM attributes map computed for inline #354.

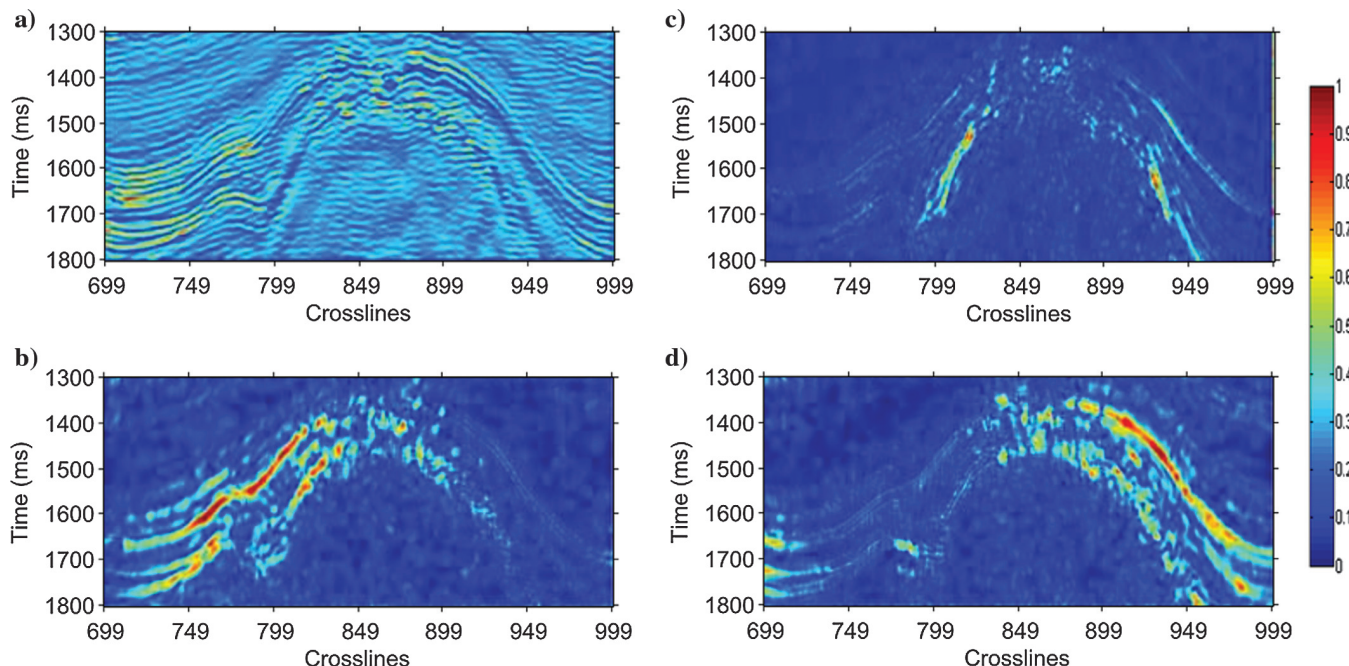


**Figure 3.** Gabor-filter attributes map for inline #354.

tensor except one. In the case of a third-order tensor, the column, row, and depth corresponds to the modes 1, 2, and 3 fibers of the tensor, respectively. For 3D seismic data, the mode-1 represents crossline, mode-2 represents inline, and mode-3 represents time information. Slices are 2D structures, extracted from a higher order tensor, by fixing every index except two. We can form three structure of slices, i.e., horizontal, lateral, and frontal from a third-order tensor by fixing  $I$ ,  $J$ , and  $K$  respectively. In Figures 5 and 6, we show the decomposition of a third-order tensor into fibers and slices.

To extract useful information from higher order tensors, such as singular value-based features, matricizing/unfolding of tensors needs first to be performed. The mode- $n$  matricizing of a tensor, denoted as  $A_{(n)}$ , is done by aligning mode- $n$  fibers of tensor and concatenating them to form a 2D matrix. The resultant unfolded matrix is used for HOSVD. The matricizing of a third-order tensor is defined as

$$\begin{aligned} A_{(1)} &= [c_{11}^1 \ c_{12}^1 \ \dots \ c_{1j}^1 \ c_{21}^1 \ \dots \ c_{2j}^1 \ \dots \ c_{kj}^1], \\ A_{(2)} &= [c_{11}^2 \ c_{12}^2 \ \dots \ c_{1i}^2 \ c_{21}^2 \ \dots \ c_{2i}^2 \ \dots \ c_{ki}^2], \\ A_{(3)} &= [c_{11}^3 \ c_{12}^3 \ \dots \ c_{1j}^3 \ c_{21}^3 \ \dots \ c_{2j}^3 \ \dots \ c_{ij}^3]. \end{aligned} \quad (7)$$

Figure 7 shows an example of seismic volume unfolded across inline and crossline directions.

The singular-value decomposition (SVD) of a matrix is a very useful tool in many applications. A 2D matrix  $X \in \mathbb{R}^{I \times J}$ , with  $I \geq J$ , can be expressed using SVD as follows:  $X = USV^T$ , where  $U \in \mathbb{R}^{I \times I}$  and  $V \in \mathbb{R}^{J \times J}$  are the orthogonal left and right singular matrices and  $S \in \mathbb{R}^{I \times J}$  is a diagonal matrix containing  $J$  singular values, such that  $\sigma_1 \geq \sigma_2 \geq \dots \geq \sigma_J$ .

HOSVD is used to decompose tensors of third or higher order. The  $n$ th-order tensor is first unfolded using the matricizing operation discussed above. SVD is then computed for each unfolded matrix. For the third-order tensor, SVD is computed for three unfolded matrices, i.e.,  $A_{(1)}$ ,  $A_{(2)}$ , and  $A_{(3)}$ :

$$\begin{aligned} A_{(1)} &= U^{(1)}S^{(1)}(V^{(1)})^T, \\ A_{(2)} &= U^{(2)}S^{(2)}(V^{(2)})^T, \\ A_{(3)} &= U^{(3)}S^{(3)}(V^{(3)})^T, \end{aligned} \quad (8)$$

where  $S^{(i)}$  is the diagonal matrix containing the singular values for mode- $i$  unfolded matrix. From  $S^{(i)}$ , we compute the following attributes:

#### Trace attribute

The singular values of the matrix  $S^{(i)}$  are used to obtain the trace attribute:

$$\text{Trace}_{\sigma}^{(i)} = \sum \text{diag}(S^{(i)}) = \sum_j \sigma_j^{(i)}, \quad (9)$$

where  $\sigma_j^{(i)}$ s are the singular values of the matrix  $S^{(i)}$ . Strong reflections from the salt domes create strong amplitudes across the boundary, whereas the texture inside salt areas and outside the salt boundary is homogeneous. This can be seen in Figure 8a. Therefore, the trace attribute gives large values along the boundary and low values for nonboundary regions.

#### Largest singular value

The largest singular value attribute is computed as

$$\sigma_l^{(i)} = \max(\text{diag}(S^{(i)})), \quad (10)$$

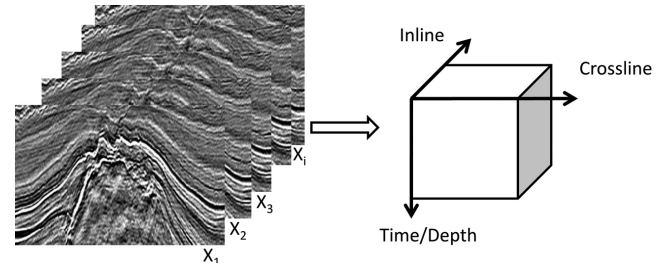


Figure 4. The 3D seismic data as third-order tensor.

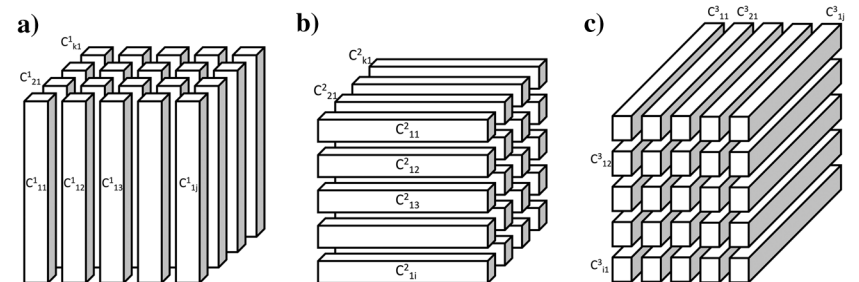


Figure 5. Fibers modes: (a) crossline, (b) inline, and (c) time.

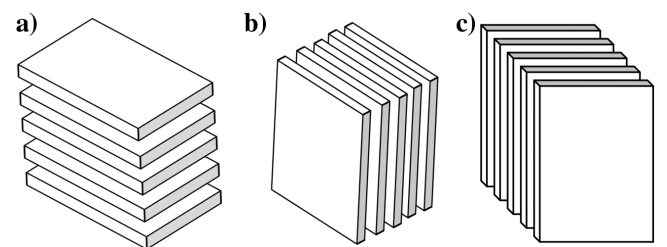


Figure 6. Slices: (a) horizontal, (b) lateral, and (c) frontal.

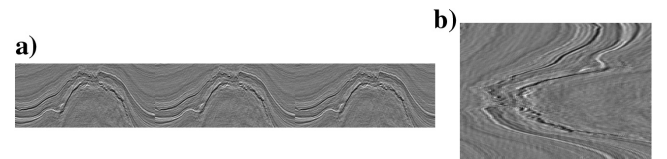


Figure 7. The 3D seismic volume unfolded across (a) crossline and (b) inline.

where  $\sigma_l^{(i)}$  is the largest singular value. Salt boundaries are often represented by strong edges in seismic data. The proposed largest singular value attribute represents edge strength in a chosen volume. The value of this attribute is high for salt boundaries represented by strong edges and weak for surrounding areas.

The trace attribute is more sensitive to texture variations as compared with the largest singular value attribute. Therefore, the trace attribute gives high value even for the small variations across the salt boundary. However, the trace attribute is also expected to highlight small variations in salt and non-salt regions that are not part of the boundary.

#### Coherence attribute

The coherence attribute is the ratio of the trace attribute and the largest singular attribute. The coherence attribute is computed as

$$C_{\sigma}^{(i)} = \frac{\sigma_l^{(i)}}{\text{Trace}_{\sigma}^{(i)}}. \quad (11)$$

The coherence attribute gives the contrast information present in seismic slices. The ratio is high for homogeneous textures because the first singular value is dominant compared with the rest. Therefore, this attribute exhibits strong values for the smooth areas and low values across the salt boundaries where we usually have high amplitude variations.

In Figures 8, 9, and 10, we show the trace attribute, the largest singular value attribute, and the coherence attribute maps computed for inline #354. The SVD was computed on subcubes of the original seismic data of size  $5 \times 5 \times 3$  samples. We see that the attribute ex-

tracted from  $S^{(1)}$  (across inline) and  $S^{(2)}$  (across cross-line) gives a very good result. However, the trace, largest singular value, and coherence attribute computed from  $S^{(3)}$  (across time) do not differentiate accurately between the salt boundary and other regions. This is mainly because of the geologic structure of the salt dome in our data set.

#### Feature ranking using an information theoretic model

The accuracy and complexity of a dictionary-based classifier depend on the relevance and number of features used for classification. To get the optimal set of features, we use an information theoretic-based model. We rank the features in order of their significance and select the  $K$  most important features that provide maximum accuracy. The value of  $K$  is chosen by experimental analysis. In this work, we use three information theoretic models, mRMR, MIFS, and JMI, for feature ranking. We discuss the results of three models and select the most important and relevant features for salt-boundary detection.

The MIFS criterion, proposed by Battiti (1994), iteratively creates the feature set by selecting the feature with highest  $J_{\text{mifs}}$  score in every iteration:

$$J_{\text{mifs}} = I(X_k; Y) - \beta \sum_{X_j \in S} I(X_k; X_j), \quad (12)$$

where  $S$  is the set that includes currently selected features,  $Y$  is the class label,  $X_k$  is the  $k^{\text{th}}$  feature. The function  $I(X; Y)$  is the mutual information between  $X$  and  $Y$ :

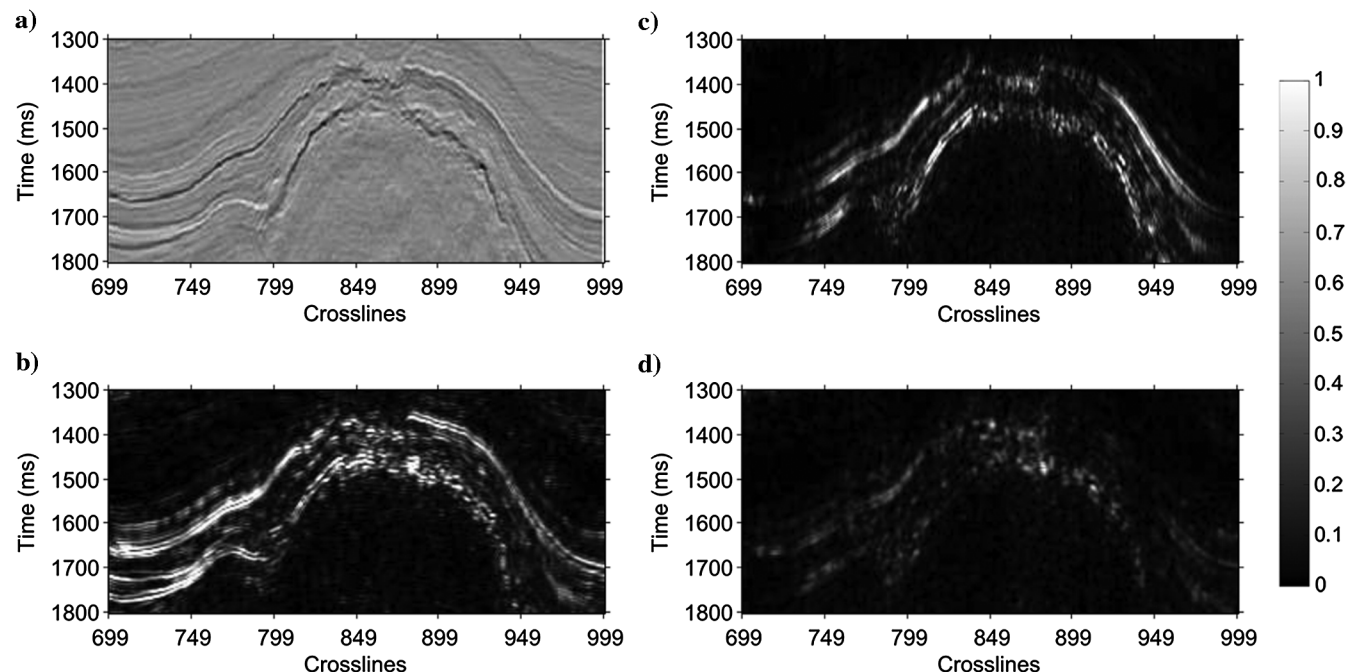


**Figure 8.** (a) Inline #354 (F3 block), and (b-d) trace-attribute maps computed across inline  $S^{(1)}$ , crossline  $S^{(2)}$ , and time  $S^{(3)}$ .

$$I(X; Y) = \sum_{x \in X} \sum_{y \in Y} p(x, y) \log \frac{p(x, y)}{p(x)p(y)}, \quad (13)$$

where  $p(x, y)$  is the joint probability mass function and  $p(x)$  and  $p(y)$  are marginal probabilities. The first term,  $I(X_k; Y)$ , in  $J_{\text{mifs}}$  maximizes the feature relevance. The second term is introduced to ensure low correlations with the features already selected in  $S$ . Iteratively, the

features are ranked in the order best to worst. By selecting different values of  $\beta$ , we can have different feature selection criterion. Choosing  $\beta = 0$  will result in selecting features independently, the criterion is also known as mutual information maximization. For most of the feature selection applications, the optimal value of  $\beta$  is one (Battiti, 1994). For our experiments, we have also used  $\beta = 1$ . The problem with the MIFS criterion is that as the set  $S$  grows, the second term with summation will

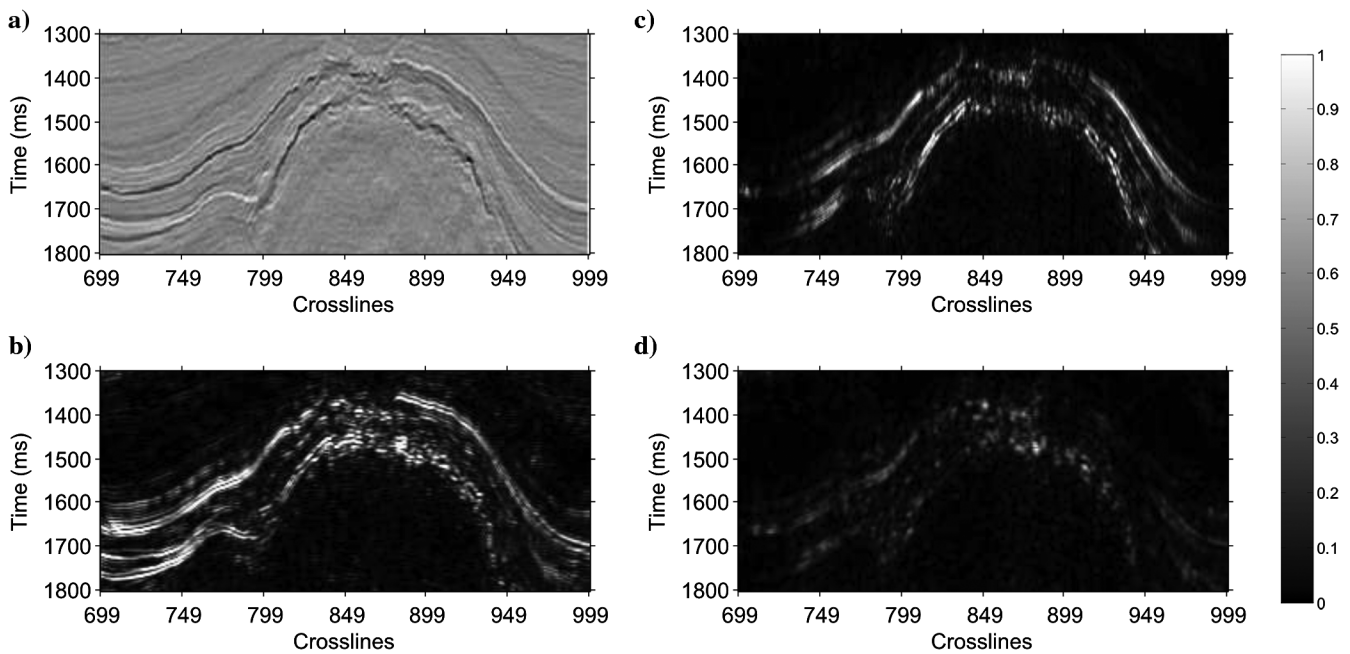


**Figure 9.** (a) Inline #354 (F3 block), and (b-d) largest singular value attribute maps computed across inline  $S^{(1)}$ , crossline  $S^{(2)}$ , and time  $S^{(3)}$ .

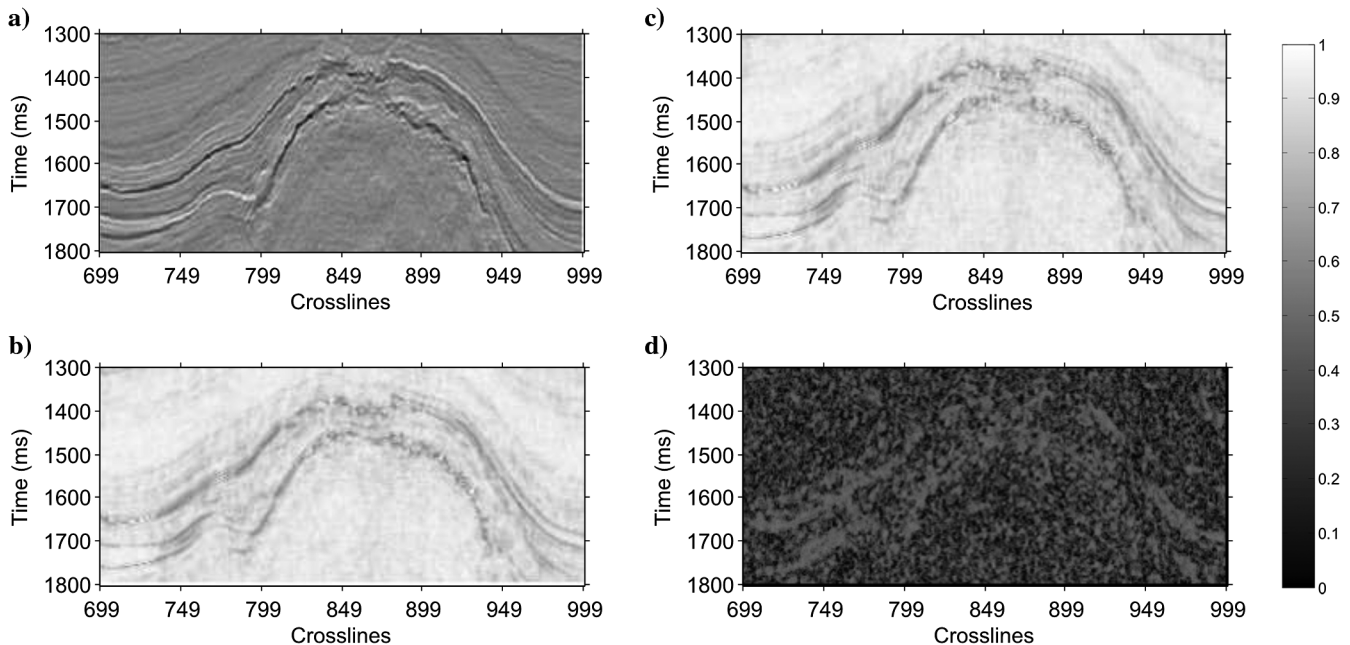


**Figure 10.** (a) Inline #354 (F3 block), and (b-d) coherence-attribute maps computed across inline  $S^{(1)}$ , crossline  $S^{(2)}$ , and time  $S^{(3)}$ .

give a large value as compared with the first term. For large  $S$ , the first term will have no or very little contribution in feature ranking.

The mRMR criterion, proposed by Peng et al. (2005), is similar to MIFS. The  $\beta$  coefficient in mRMR is in inverse relation with the size of current feature selection set. This choice of  $\beta$  overcomes the limitation of MIFS and limits the second term even when  $S$  becomes large. The selection criteria for mRMR is given as

$$J_{\text{mRMR}} = I(X_k; Y) - \frac{1}{|S|} \sum_{j \in S} I(X_k; X_j). \quad (14)$$

For large feature sets, earlier work has shown that the performance of the mRMR is superior to the MIFS ( $\beta = 1$ ). However, in the case of small feature sets, the mRMR is not always expected to perform better than the MIFS. In our experiments, the size of feature set is small (16 attributes). Therefore, we opted to test both algorithms for feature ranking.

As we know, correlation does not always imply redundancy. The inclusion of correlated features can be useful provided correlation within classes is stronger than the overall correlation. Yang and Moody (1999) and Meyer et al. (2008) propose the JMI feature selection criterion, which also considers the interclass and intraclass correlation. The JMI criterion selects the new feature only if it complements the existing features in set  $S$ . The selection criterion for JMI is given as

$$J_{\text{JMI}} = \sum_{j \in S} I(X_k X_j; Y). \quad (15)$$

**Table 1. Feature ranking using mRMR, MIFS, and JMI selection criterion.**

Attribute	MIFS	mRMR	JMI
GLCM contrast	4	4	5
GLCM entropy	11	11	12
GLCM energy	5	5	9
Gabor attribute ( $\theta = 0$ )	13	13	14
Gabor attribute ( $\theta = pi/4$ )	3	3	3
Gabor attribute ( $\theta = pi/2$ )	7	7	6
Gabor attribute ( $\theta = 3pi/4$ )	10	10	8
Trace attribute ( $\text{Trace}_{\sigma}^{(1)}$ )	2	2	2
Trace attribute ( $\text{Trace}_{\sigma}^{(2)}$ )	1	1	1
Trace attribute ( $\text{Trace}_{\sigma}^{(3)}$ )	9	9	10
Largest singular value $\sigma_l^{(1)}$	8	8	7
Largest singular value $\sigma_l^{(2)}$	6	6	4
Largest singular value $\sigma_l^{(3)}$	12	12	11
Coherence attribute $C_{\sigma}^{(1)}$	15	15	15
Coherence attribute $C_{\sigma}^{(2)}$	14	14	13
Coherence attribute $C_{\sigma}^{(3)}$	16	16	16

After some manipulations (see Brown et al., 2012), the above relation can be written as

$$J_{\text{JMI}} = I(X_k; Y) - \frac{1}{|S|} \sum_{j \in S} I(X_k; X_j) - I(X_k X_j; Y). \quad (16)$$

Like mRMR, the JMI also selects the features independently as the size of feature set  $S$  grows. The difference here is the conditional term.

In Table 1, we show the ranking of features according to the three criteria. In Figure 11a, we show the histogram of the top ranked feature. We can see that the distributions of salt boundary and nonsalt boundary samples are almost separate and the overlapping region is very small. In Figure 11b, we show the histogram of the salt boundary and nonsalt boundary samples for the lowest ranked feature; the two distributions overlap each other completely, which illustrates that classification using this feature will give poor results.

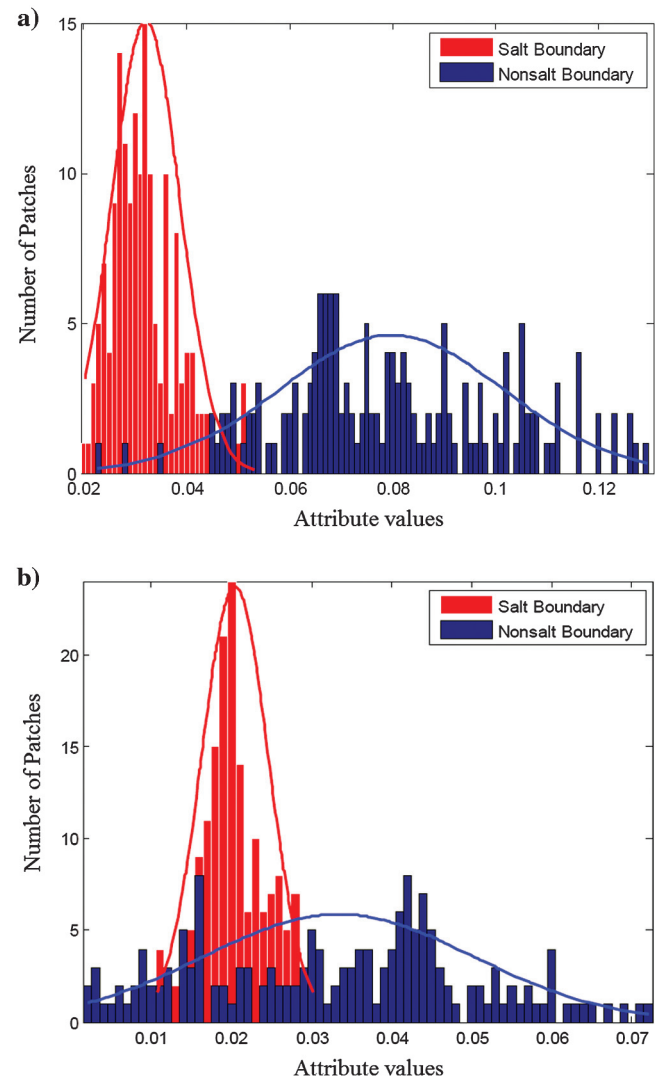


**Figure 11.** (a) Histogram of top ranked attribute (trace attribute across crossline) and (b) histogram of the lowest ranked attribute (coherence attribute across time).

Note that the feature ranking process is performed just once prior to the salt-dome detection process; therefore, it does not increase the computational complexity of the detection process.

### Classification using dictionary-based learning

Dictionary-based classifiers have the advantage of working with a minimum number of features and have shown excellent results in various texture classification problems, such as fingerprint identification, tumor segmentation, breast cancer detection, etc.

The fundamental principle of texture-based classification is to use the training features from  $n$  distinct textures covering different classes to correctly classify a given test sample. The  $n$  training feature vectors, each of length  $m$ , are stacked to construct a dictionary  $\mathbf{D} = [\mathbf{v}_1, \mathbf{v}_2, \dots, \mathbf{v}_n] \in \mathbb{R}^{m \times n}$ . The columns of the dictionary  $\mathbf{D}$  are then the features of  $n$  training textures.

For the salt-dome detection, we consider two classes of textures: (1) salt-boundary texture and (2) non-salt boundary texture. The non-salt boundary region includes the salt areas and the areas outside the salt boundary. In Figure 12, we show the samples of salt boundary and non-salt boundary patches used for dictionary learning. A dictionary  $\mathbf{D}$  is then represented as

$$\mathbf{D} = [\mathbf{D}_1 \quad \mathbf{D}_2] = [\mathbf{v}_{1,1}, \mathbf{v}_{1,2}, \dots, \mathbf{v}_{1,n_1} \mathbf{v}_{2,1}, \dots, \mathbf{v}_{2,n_2}] \in \mathbb{R}^{m \times n}, \quad (17)$$

where  $n_1$  and  $n_2$  are the number of training samples of salt boundary and non-salt boundary patches. Here,  $\mathbf{D}_1 = [\mathbf{v}_{1,1}, \mathbf{v}_{1,2}, \dots, \mathbf{v}_{1,n_1}] \in \mathbb{R}^{m \times n_1}$  is the matrix containing feature samples from the salt-boundary class, and  $\mathbf{D}_2 = [\mathbf{v}_{2,1}, \mathbf{v}_{2,2}, \dots, \mathbf{v}_{2,n_2}] \in \mathbb{R}^{m \times n_2}$  is the matrix containing feature samples from the non-salt boundary class.

A test sample  $\mathbf{y} \in \mathbb{R}^{m \times 1}$  belonging to the salt boundary class will lie in the linear span of  $\mathbf{D}_1$ , given that  $\mathbf{D}_1$  has enough training samples, and can be projected as

$$\mathbf{y} = c_{1,1}\mathbf{v}_{1,1} + c_{1,2}\mathbf{v}_{1,2} + \dots + c_{1,n_1}\mathbf{v}_{1,n_1}, \quad (18)$$

where  $c_{1,1}, c_{1,2}, \dots, c_{1,n_1}$  are the scalar values. For the complete dictionary  $\mathbf{D}$ , which contains feature vectors from both classes, the linear representation of  $\mathbf{y}$  can be rewritten as

$$\mathbf{y} = c_{1,1}\mathbf{v}_{1,1} + \dots + c_{1,n_1}\mathbf{v}_{1,n_1} + c_{2,1}\mathbf{v}_{2,1} + \dots + c_{2,n_2}\mathbf{v}_{2,n_2}, \quad (19)$$

where  $c_{2,1}, c_{2,2}, \dots, c_{2,n_2}$  have zero values. Therefore,

$$\mathbf{y} = \mathbf{D}\mathbf{x}, \quad (20)$$

where  $\mathbf{x} = [c_{1,1}, c_{1,2}, \dots, c_{1,n_1}, 0, 0, \dots, 0]$  is a vector whose only nonzero entries are the ones that are associated with the salt-boundary class.

Give a test sample  $\mathbf{y}$  from a salt-boundary class and the dictionary  $\mathbf{D}$ , we first compute  $\mathbf{x}$ . The system  $\mathbf{y} = \mathbf{D}\mathbf{x}$  is underdetermined and  $\mathbf{x}$  is sparse; therefore, we can solve the following  $\ell_1$ -minimization problem:

$$\hat{\mathbf{x}} = \operatorname{argmin} \|\mathbf{x}\|_1 \quad \text{subject to } \mathbf{D}\mathbf{x} = \mathbf{y}. \quad (21)$$

Solving the  $\ell_1$ -norm minimization problem is computationally intensive. The cost of the solution using linear programming (LP) is of order  $O(n^3)$ , which is extremely slow for seismic data of very large size. Alternatively, other approximation methods, such as the orthogonal matching pursuit algorithm (Donoho et al., 2006), and homotopy (ul Haq et al., 2012) can be used.

For an exact match, the nonzero entries in  $\hat{\mathbf{x}}$  will be associated with the columns of  $D$  corresponding to the salt-boundary patches only. For all the other columns, the entries will be zero. However, this is not true due to limited number of training samples. Therefore, to classify  $y$ , we can sum the entries of  $\hat{\mathbf{x}}$  associated with each class and select the class, which gives the maximum value:

$$r_i(y) = \sum_{k_i} \alpha(\hat{x}_i), \quad (22)$$

$$\text{class}(y) = \operatorname{argmax}_i r_i(y), \quad (23)$$

where  $\alpha(\hat{x}_i)$  contains the entries of the estimated vector  $\hat{\mathbf{x}}$  associated with class  $i$ . For our case, we will select the maximum from  $r_1(y)$  and  $r_2(y)$ , where  $r_1(y)$  is the sum of the elements of  $\hat{\mathbf{x}}$  associated with salt boundary and  $r_2(y)$  is the sum of elements of  $\hat{\mathbf{x}}$  associated with non-salt boundary. Algorithm 1 describes the construction of the dictionary.

Based on the above dictionary, we outline our proposed dictionary classification algorithm (Algorithm 2) for salt-dome detection.

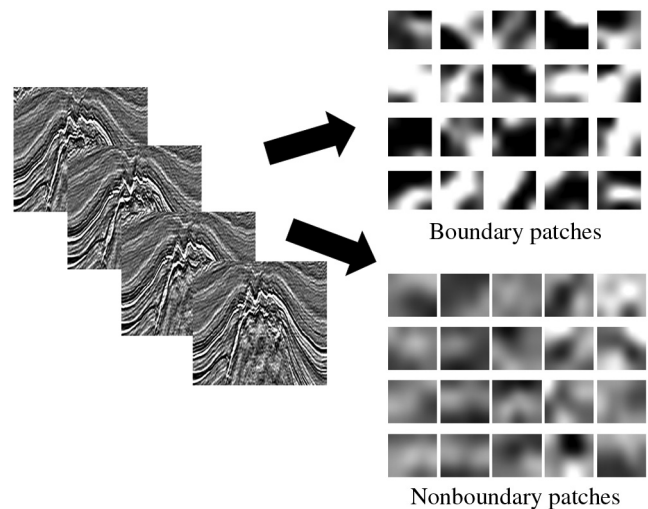


**Figure 12.** Salt boundary and non-salt boundary patches extracted from training data.

The dictionaries constructed using powerful and relevant feature sets can be reused for salt-dome detection across different seismic surveys. The concept of dictionaries can also be adopted to detect other types of events, such as horizons and faults.

### **Accurate salt-boundary detection using edge strength and largest eigenvalue**

Dictionary-based classifiers, discussed in the previous section, classify the boundary patches with good accuracy. The size of each patch is  $N \times N$  samples, where  $N \geq 3$ . To estimate the boundary from the classified patches, we need a further refinement step. In Amin et al. (2015), the boundary is extracted from the classified patches by just considering the lower part (row) of each patch. The results, however, were not refined. Another approach is to take the center row of each patch and estimate the salt boundary. A third option is to consider the upper part of each patch as the boundary of salt dome. All of these three mentioned approaches may work for some slices, but may not produce the desired results for other slices. In this work, we propose a refining step, based on the energy and the edge strength, to estimate the salt boundary accurately within a patch. For the classified patches, we compute the energy using the eigenvalue attribute as discussed in Berthelot et al. (2012) and the edge strength using the Sobel operator. We select the points that give the maximum energy and edge values for detecting the salt boundary.

We have shown in our earlier work (Amin and Deriche, 2015a) that texture-based attributes provide better accuracy for salt-dome detection as compared with edge-based methods. However, once the initial boun-

dary is estimated, the edge strength can efficiently be used to refine the boundary. Therefore, in this workflow, we also use the texture-based attributes for the classification of patches and edge and energy values to get the accurate refined boundary.

The eigenvalue attribute is computed using the covariance matrix obtained from the gradients in the  $x$ -,  $y$ -, and  $z$ -directions. The value of this attribute will be high for the salt boundary and low for the surrounding areas. Therefore, this attribute can assist in detecting the salt boundary accurately within a patch. The covariance matrix is computed as

$$C = \begin{bmatrix} C_{xx} & C_{xy} & C_{xz} \\ C_{yx} & C_{yy} & C_{yz} \\ C_{zx} & C_{zy} & C_{zz} \end{bmatrix}, \quad (24)$$

$$C_{ab} = \frac{1}{N^3} \sum_{x,y,z} (G_a(x, y, z) - \mu_a)(G_b(x, y, z) - \mu_b), \quad (25)$$

where  $N$  is the window size ( $N = 9$  for  $3 \times 3$  windows),  $G_a$  and  $G_b$  are the gradients in the directions  $a$  and  $b$ , and  $\mu_a$  and  $\mu_b$  are the means in the  $a$  and  $b$  directions, respectively. From the covariance matrix, we get the eigenvalue attribute:

$$\lambda_1 = \max(\lambda_i), \quad (26)$$

where  $\lambda_i$ 's are the eigenvalues of the covariance matrix. The largest eigenvalue  $\lambda_1$  gives the energy information for each pixel. We use this value along with the edge strength to get the desired salt boundary.

For the edge strength, we use the Sobel edge detector, which computes spatial gradients of an image and enhances regions of high frequency that represent edges. The convolution operators for the Sobel edge detector in the  $x$ - and  $y$ -directions are given as

$$G_x = \begin{bmatrix} -1 & 0 & 1 \\ -2 & 0 & 2 \\ -1 & 0 & 1 \end{bmatrix}, \quad (27)$$

---

### **Algorithm 1. Dictionary construction.**

---

1. From the available seismic data set, select  $n$  patches of size  $L \times L$  samples for training.
  2. Compute  $K$  GLCM, Gabor, and HOSVD-based features for each training patch.
  3. Select  $m$  features, such that  $m < K$ .
  4. Stack the  $m$  feature samples for training patches to create a dictionary  $\mathbf{D} \in \mathbb{R}^{m \times n}$ .
- 

---

### **Algorithm 2. Dictionary-based classification.**

---

1. Create a dictionary from the given training data for two classes: (1) class 1: salt boundary, and (2) nonsalt boundary (use Algorithm 1).
  2. Divide the input test inline into  $L \times L$  nonoverlapping patches.
  3. For each patch, compute and select  $m$  GLCM, Gabor, and HOSVD-based features such that  $\mathbf{y}_i \in \mathbb{R}^m$ .
  4. For each patch, solve the  $\ell_1$ -minimization problem  $\hat{\mathbf{x}} = \text{argmin} \|\mathbf{x}\|_1$  subject to  $\mathbf{D}\mathbf{x} = \mathbf{y}$ .
  5. Compute  $r_1(y) = \sum_{k_1} \alpha(\hat{x}_1)$  and  $r_2(y) = \sum_{k_2} \alpha(\hat{x}_2)$ .
  6. Identify the class of all the patches using  $\text{class}(y) = \text{argmax}\{r_1(y), r_2(y)\}$ .
-

$$G_y = \begin{bmatrix} -1 & -2 & -1 \\ 0 & 0 & 0 \\ 1 & 2 & 1 \end{bmatrix}. \quad (28)$$

Although the Sobel operator gives better results as compared with other edge detectors, considering the gradient map only in the  $x$ - and  $y$ -directions may not give accurate results along the diagonal directions of salt-dome boundaries. To improve the performance of the Sobel edge detector, we include the diagonal directions ( $45^\circ$  and  $135^\circ$ ) along with the  $x$ - and  $y$ -directions. The convolution operators for the Sobel edge detector in the diagonal directions are given as

$$G_{45} = \begin{bmatrix} -2 & -1 & 0 \\ -1 & 0 & 1 \\ 0 & 1 & 2 \end{bmatrix}, \quad (29)$$

$$G_{135} = \begin{bmatrix} 0 & -1 & -2 \\ 1 & 0 & -1 \\ 2 & 1 & 0 \end{bmatrix}. \quad (30)$$

The magnitude of the total gradient is now computed as

$$G = \sqrt{G_x^2 + G_y^2 + G_{135}^2 + G_{45}^2}. \quad (31)$$

The energy value and the edge-strength value are accumulated, and the points with maximum values in the classified patches are selected as the boundary points.

The refining step introduced here has two advantages: First, the boundary is estimated accurately within each patch and we get refined results when compared with the other patch-based methods. Second, we can choose different patch sizes ( $N \times N$  samples). The more accurate features can be estimated using a large patch size (a large value of  $N$ ). Patch-based methods (Amin et al., 2015), without the refining step, are sensitive to the patch size because the shape of the detected salt boundary depends largely on the size and location of patches. A more accurate and refined boundary is obtained for the small patches. However, the features estimated from the small patches may not be very accurate. In our work, we use a large patch size to estimate good features. For the final salt-dome boundary, we use the refining step based on the energy value and the edge strength.

## Experimental results

We tested our salt-dome detection method on the Netherlands offshore F3 block acquired in the North Sea for oil and gas exploration. The survey covers an area of  $24 \times 16\text{ km}$ . The inline range is from 100 to 750, the crossline range is 300–1250, the time direction ranges from 0 to 1848 ms sampled at every 4 ms, and the bin size is 25 m in inline and crossline directions.

The data set contains important geologic features, such as salt dome, faults, and bright spots.

We selected 100 inline sections each of size  $130 \times 300$ . The dictionary was created using 400 training patches of size  $N \times N$  samples. The number was chosen to have enough data for training the classifier, without overfitting the overall model. The training patches were selected equally from the salt boundary and non-salt boundary classes. For each patch, the proposed algorithm computes GLCM attributes, Gabor-filter attributes, and HOSVD-based attributes. Separate inlines are used for training and testing.

The ground truth labels used for testing were obtained in collaboration with the geophysics expert, Dr. A. Al Suhail, who worked extensively with seismic data. The interpretation process was blind. The pool of experts to validate our results will be expanded in future work to reduce the effects of bias.

## Feature selection using MIFS, mRMR, and JMI

We rank the attributes, computed for each patch, using the MIFS, the mRMR, and the JMI criterion and select the top  $K$  features. The value of  $K$  is chosen empirically. From experiments, we found that the top seven ranked attributes provide best results for salt-dome detection. In Figure 13, we show the classification accuracy computed for different values of  $K$ . We observe that the maximum accuracy is achieved for  $K = 7$ . As the value of  $K$  increases beyond seven, we observe a dip in the accuracy value. This is because the low-ranked attributes do not provide any new information; rather, they increase the confusion (the curse of dimensionality), which results in a low accuracy value. For the classification accuracy, we have used the  $F$ -measure value, which is most commonly used evaluation metric in the image segmentation problems (see equations 31–33).

In Table 2, we show the top seven ranked attributes using mRMR, MIFS, and JMI features selection criteria. We observe that the top seven ranked features using mRMR and MIFS are the same. This is because the size of set  $S$  is not large. Therefore, the second term in MIFS does not limit the effect of the first term. We show in Figure 14 the classification accuracy of the salt boun-

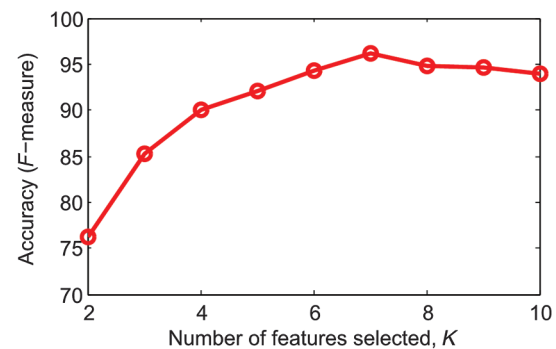


Figure 13. Classification accuracy  $K = 2, 3, \dots, 10$ .

dary detected for inlines #350–#359 using the proposed method with feature ranking based on mRMR, MIFS, and JMI. We select the top seven attributes ranked by mRMR, MIFS, and JMI. The proposed algorithm using the JMI selection criteria gives an average accuracy of 96.5%, which is 0.4% higher than the proposed method using the mRMR or MIFS criterion. Therefore, for further experiments, we have used the top seven attributes ranked by the JMI criterion.

### Optimal patch size for training and testing

The selection of patch size ( $N \times N$  samples) plays an important role in extracting good features for salt-dome detection. The accuracy of the features extracted from the GLCM, and those computed from the Gabor filter, depends on the window (patch) size. The value of  $N$  is also important in estimating the final boundary of salt dome. The introduction of a refining step based on the energy value and edge strength gives us the ability to choose a large value of  $N$ . In Figure 15, we show the classification accuracy computed for different patch sizes. We see that the maximum accuracy is achieved for  $N = 7$ . This is because for  $N < 7$ , the features extracted from the patches are not very accurate as the size of patch is small. For  $N > 7$ , the accuracy decreases because the features extracted from large patches do not include the local information. In addition, there are many other points in inline #389 in which the salt boundary is rep-

top including the first/inner layer only, thus ignoring the outer layer (Amin and Deriche, 2016). The final boundary is then obtained by linking the missing points using the joining line followed by the smoothing operation. Figure 16c shows the ground truth and the salt boundary detected for the inline #354 using the proposed method. The green boundary here is the ground truth, and red is the boundary produced by the proposed method. We see that the proposed method is able to outline the boundary with good accuracy.

Two more examples are provided in Figure 17 for inlines #360 and #389 using the proposed method. The salt boundaries produced by the proposed method are very close to the ground truth. The boundaries at the end of salt dome in inlines #360 and #389 are represented by weak amplitudes. In addition, there are many other points in inline #389 in which the salt boundary is rep-

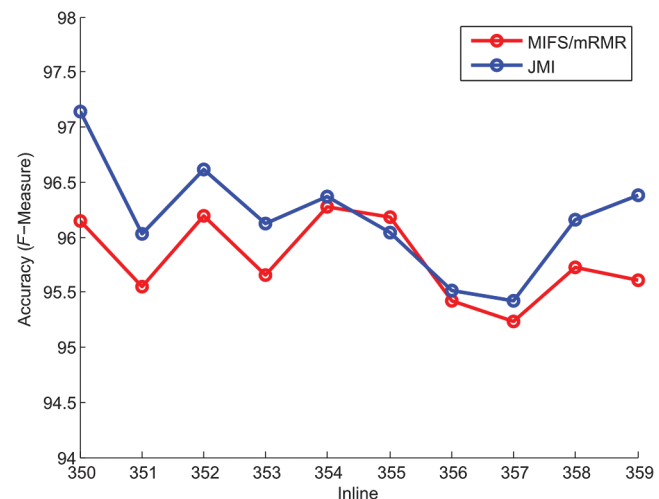


**Figure 14.** Classification accuracy using MIFS/mRMR and JMI for  $K = 7$ .

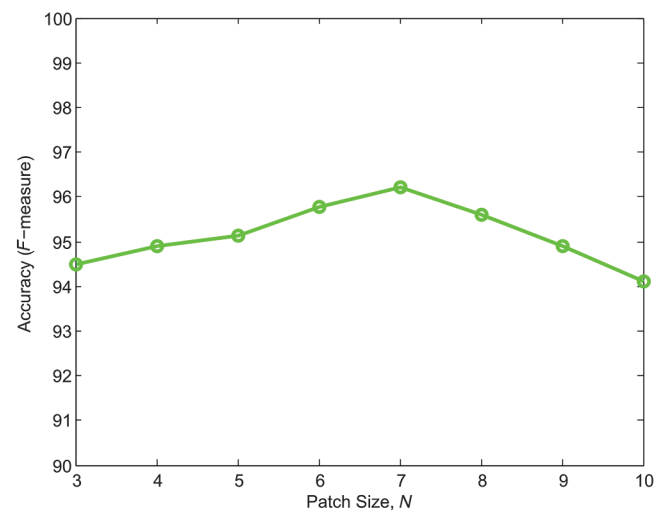


**Figure 15.** Classification accuracy  $N = 3, 4, \dots, 10$ .

resented by very weak reflections. In Figure 17b and 17d, we observe that the proposed method is able to delineate the salt boundaries accurately. This is due to the optimal feature set created using ranking models and powerful HOSVD-based attributes.

We compared the performance of our method with the edge-detection-based method (Aqrabi et al., 2011), the texture-attributes-based method (Berthelot et al., 2013), the hybrid edge, and texture-based method (Amin and Deriche, 2015a), the dictionary-based classi-

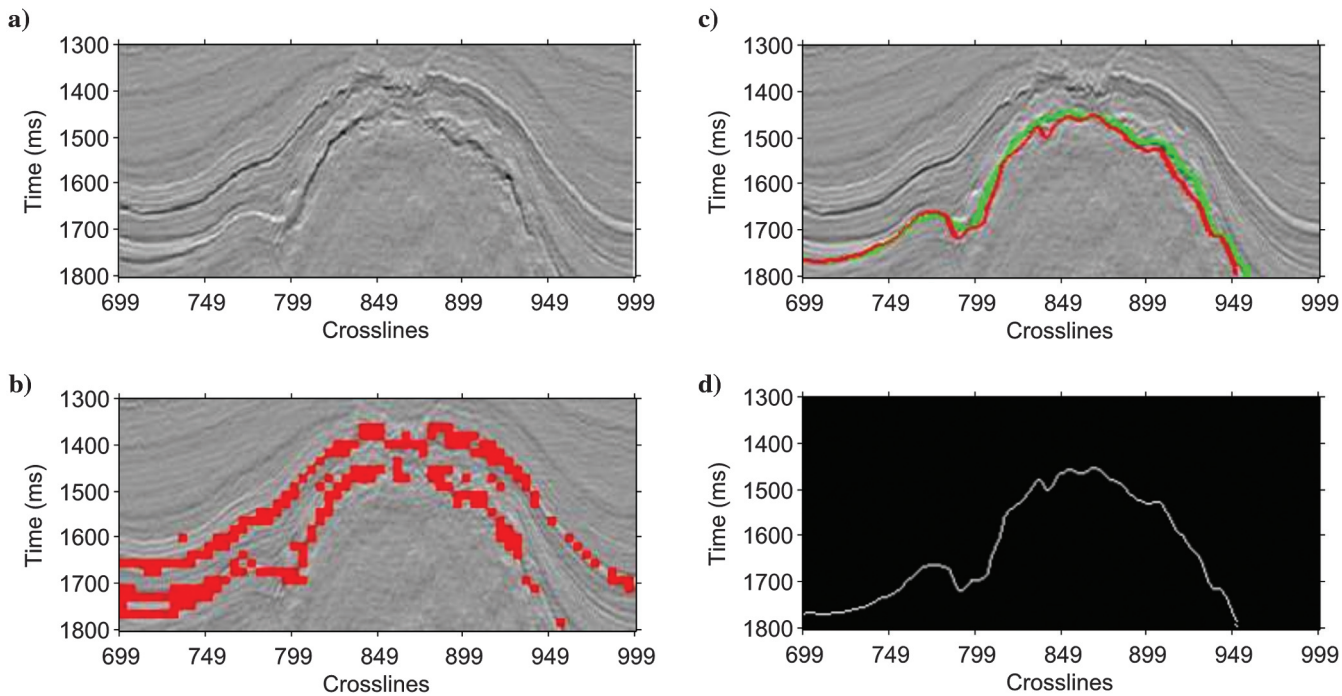


**Figure 16.** (a) Inline #354, (b) identified salt-boundary patches, (c) ground truth (green), detected salt boundary (red), and (d) outline of the detected boundary.

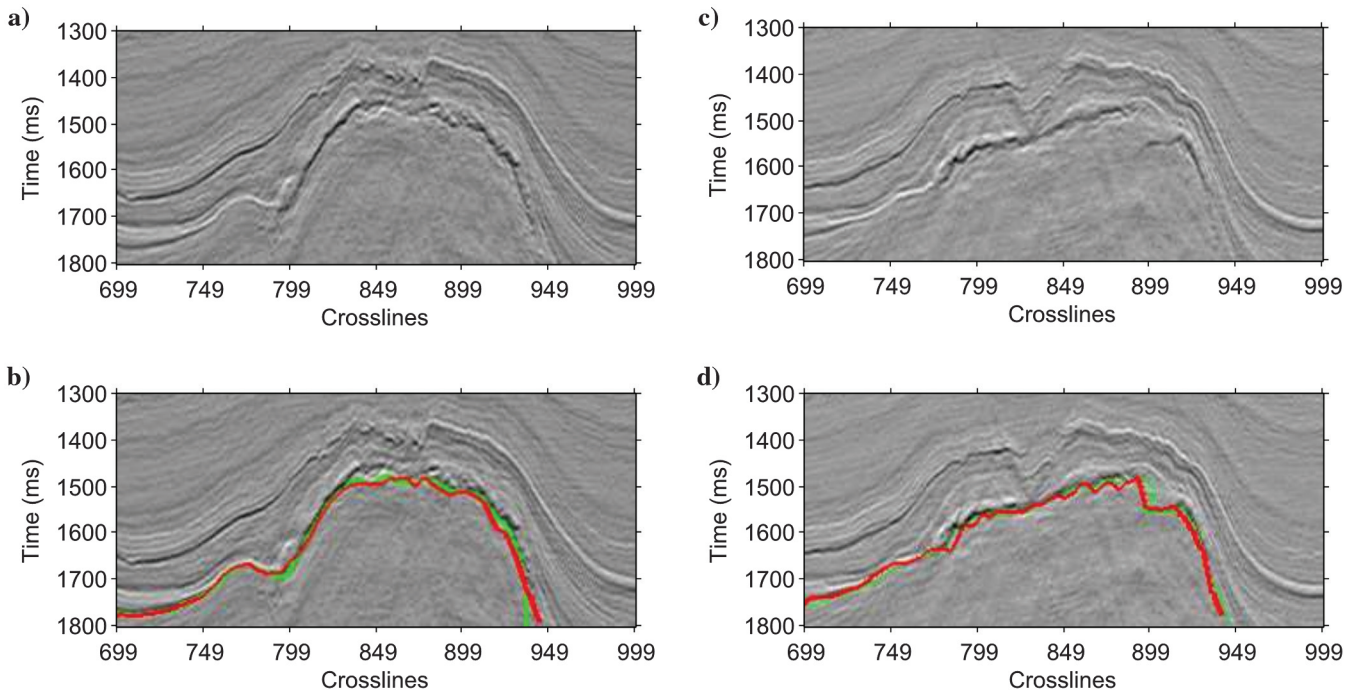


**Figure 17.** (a) Inline #360, (b) salt boundary detected for the inline #360, (c) inline #389, and (d) salt boundary detected for the inline #389.

fication method (Amin et al., 2015), and the 3D GoT method (Shafiq et al., 2015b). Sobel edge detector is used for the Aqrawi method. The texture-based method (Berthelot et al., 2013) uses the attributes computed from the GLCM, the Gabor filter, and the eigenstructure. Figure 18 shows the classification results using the proposed and other methods. The green boundary here is the ground truth, red is the boundary produced by the proposed method, blue is the boundary produced by the Aqrawi et al. (2011) method, cyan is the boundary produced by the Berthelot et al. (2013) method, purple is the boundary produced by the Amin and Deriche (2015a), yellow is the boundary produced by the Amin et al. (2015) method, and black is the boundary produced by the Shafiq et al. (2015b) method. We can see that the boundary produced by our algorithm is very close to the ground truth. The boundary produced by the Berthelot et al. (2013) method deviates from the ground truth at various points because this method is sensitive to the features used for classification. The Aqrawi et al. (2011) method is not able to detect the points at the end of salt dome where the boundary

is not represented by a strong edge. The Amin and Deriche (2015a) method, which combines edge and texture attributes, is able to trace the boundary accurately except for the diagonals and the end points of the salt dome. The Amin et al. (2015) method considers the lower portion of classified patches as a salt boundary; therefore, this method is not able to produce smooth results as can be seen in Figure 18. The Shafiq et al. (2015b) method, which measures the texture dissimilarity between two neighboring cubes, misses some points at the start and end of the salt dome and falsely classifies some part of the nonsalt region as the salt dome. The results produced by the proposed method are much better in terms of accuracy than the other salt-dome detection methods. Figure 19 shows the boundary outline produced using the proposed method and the other methods.

In Table 3, we show the average classification accuracy (the normalized Frechet distance) of salt boundaries, computed for inlines #350 to #399, using the proposed method and the other methods. The proposed method gives an average accuracy of 90.57%, which is

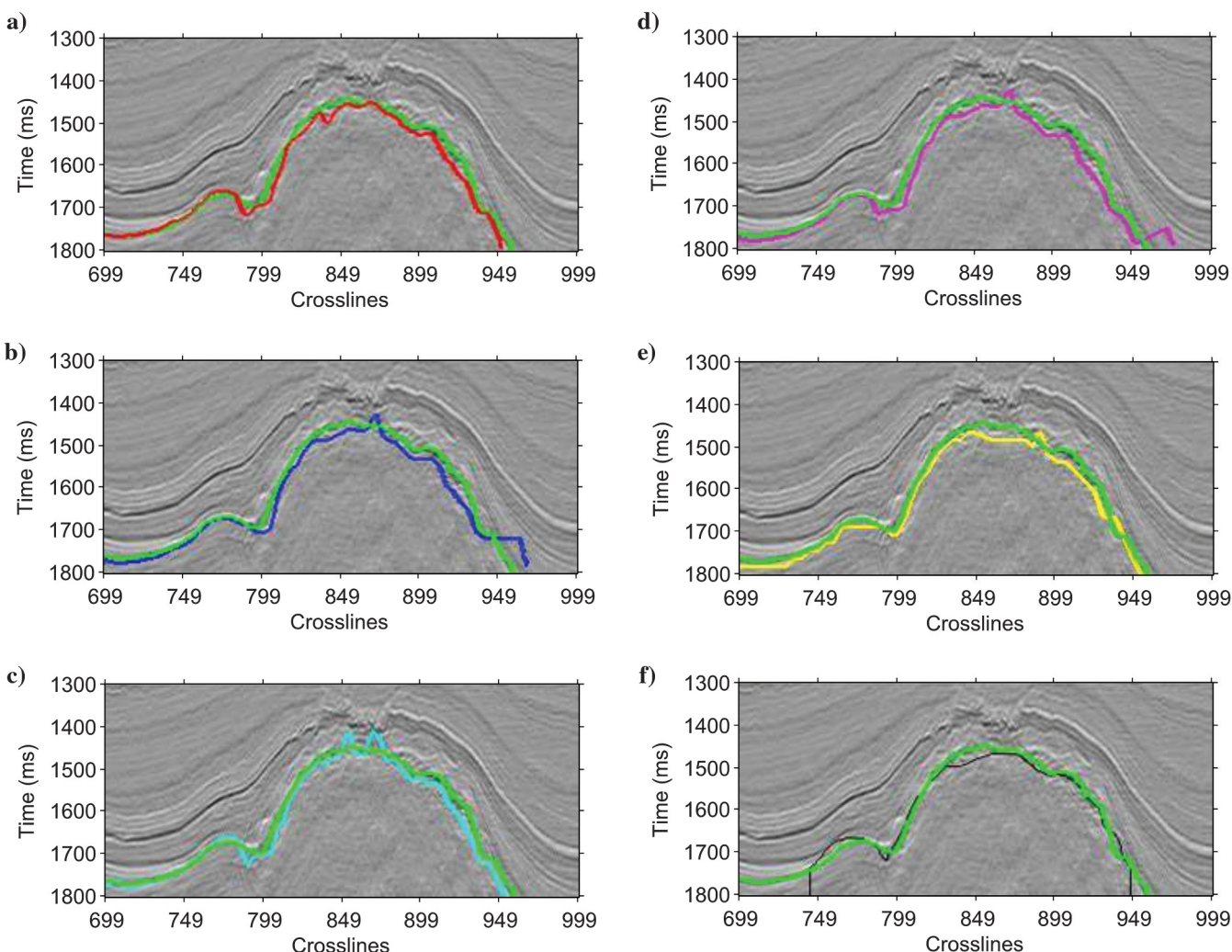


**Figure 18.** Salt boundary detected for inline #354 using (a) the proposed method, and (b-f) the other methods.

almost 4% higher than the Aqrawi et al. (2011) method, 3% higher than the Berthelot et al. (2013) method, 2% higher than the Amin et al. (2015) and Shafiq et al. (2015b) methods, and 1% higher than the Amin and Deriche (2015a) method.

Precision, recall, and *F*-measure are used commonly as objective evaluation metrics in image segmentation. To calculate these metrics, we compute the true positive (TP), the false positive (FP), the true negative (TN), and the false negative (FN) using the ground truth and the detected salt region:

- TP: salt-dome points classified correctly
- TN: nonsalt points classified correctly
- FP: nonsalt points classified as salt points
- FN: salt-dome points classified as nonsalt points.

Precision, recall, and *F*-measure are computed using

$$\text{Precision} = \frac{\text{TP}}{\text{TP} + \text{FP}}, \quad (32)$$

$$\text{Recall} = \frac{\text{TP}}{\text{TP} + \text{FN}}, \quad (33)$$

$$F - \text{Measure} = 2 \times \frac{\text{Precision} \times \text{Recall}}{\text{Precision} + \text{Recall}}. \quad (34)$$

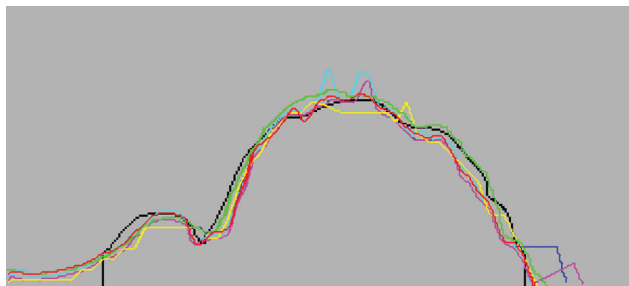


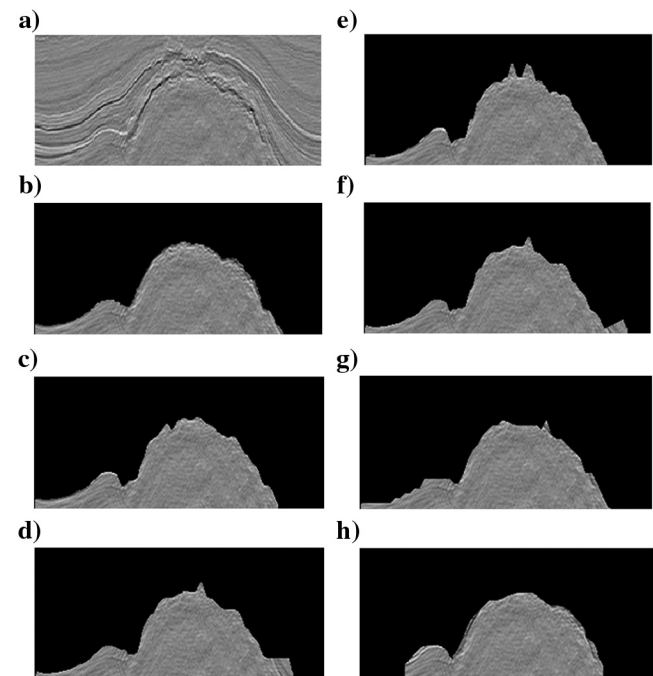
**Figure 19.** Ground truth (green); salt-boundary outline produced for inline #354 using the proposed method (red), the Aqrawi et al. (2011) method (blue), the Berthelot et al. (2013) method (cyan), the Amin and Deriche (2015a) method (purple), the Amin et al. (2015) method (yellow), and the Shafiq et al. (2015b) method (black).

**Table 3. Classification accuracy.**

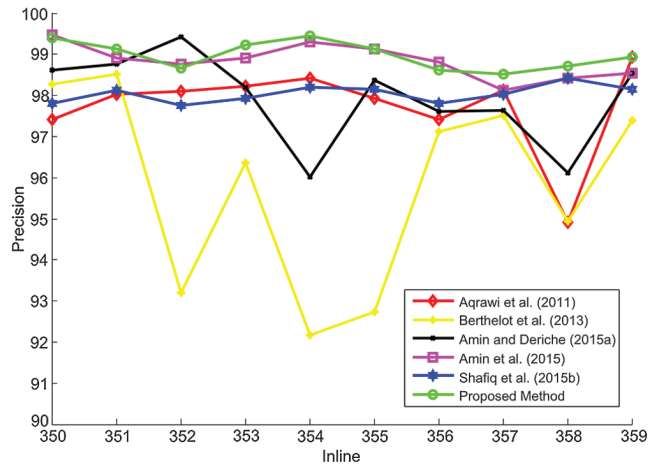
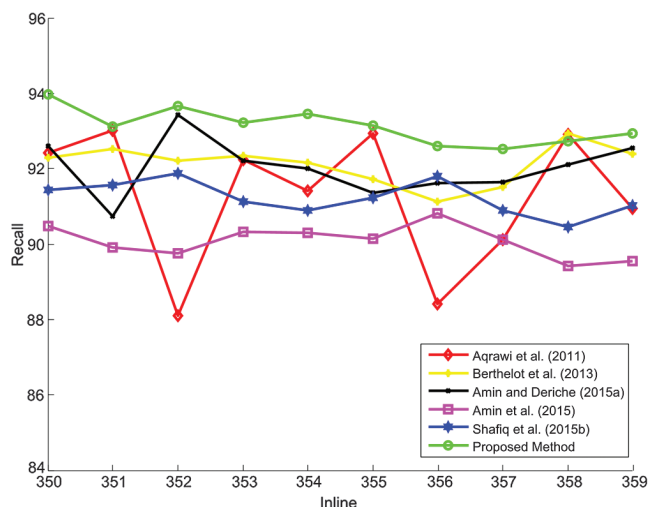
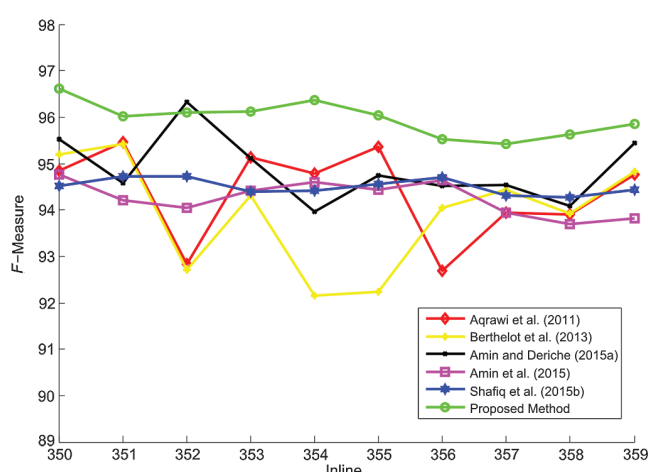
Salt-dome detection method	Average accuracy
Proposed method	90.57%
Aqrawi et al. (2011)	86.74%
Berthelot et al. (2013)	87.78%
Amin and Deriche (2015a)	89.61%
Amin et al. (2015)	88.83%
Shafiq et al. (2015b)	88.48%

In Figure 20, we show the ground truth of the salt dome and the salt regions detected using the proposed one and the other methods for inline #354. In Figures 21, 22, 23, we show and compare the precision, recall, and *F*-measure values computed for inlines #350 to #359 using the proposed method and the other methods discussed above. Precision gives the percentage of correctly classified salt points out of total classified points. We see that the proposed method gives excellent precision values for all inlines followed closely by the Amin et al. (2015) method. The Aqrawi et al. (2011) and Shafiq et al. (2015b) methods give consistent precision values for different inlines; however, the values are less than those computed for the proposed and Amin et al. (2015) method. The Berthelot et al. (2013) method misclassifies some nonsalt areas as salt, as can be seen in Figure 20. Therefore, the precision values are not consistent and vary significantly for different inlines. The Amin and Deriche (2015a) method, which combines the edge and texture attributes, gives good precision values with some inconsistency. This inconsistency is due to the over-segmented salt region produced by the texture attributes-based method.

For the second evaluation metric, i.e., recall, the proposed method gives the highest values for all inlines followed by the Berthelot et al. (2013) and Amin and Deriche (2015a) methods. The Amin et al. (2015) method gives consistent, but lowest recall values among all the methods. This is because the Amin et al. (2015) method considers the bottom pixels of each classified



**Figure 20.** (a) Inline #354, (b) ground truth, detected salt dome, (c) the proposed method, (d) the Aqrawi et al. (2011) method, (e) the Berthelot et al. (2013) method, (f) the Amin and Deriche (2015a) method, (g) the Amin et al. (2015) method, and (h) the Shafiq et al. (2015b) method.

**Figure 21.** Precision.**Figure 22.** Recall.**Figure 23.** The *F*-measure.

patch as salt boundary; therefore, the detected shape is not very accurate. The recall values, calculated for the [Aqrabi et al. \(2011\)](#) and [Amin and Deriche \(2015a\)](#) method, shows inconsistency and changes significantly for different inlines. The [Shafiq et al. \(2015b\)](#) method gives consistent but low recall values.

The third metric, *F*-measure, is used in image segmentation to find the accuracy of segmented regions. We have also used the *F*-measure to compute the classification accuracy of salt-dome detection methods. From Figure 23, we see that the proposed algorithm gives the highest *F*-measure values followed by the [Amin and Deriche \(2015a\)](#) method. The [Amin et al. \(2015\)](#) and [Shafiq et al. \(2015b\)](#) methods give consistent, but low *F*-measure values as compared with the proposed method. The [Aqrabi et al. \(2011\)](#) and [Berthelot et al. \(2013\)](#) methods give inconsistent *F*-measure values for different inlines.

In Table 4, we show the average precision, recall, and *F*-measure values computed for inlines #350–399. The average *F*-measure value obtained for the proposed method is almost 2.6% higher than the [Berthelot et al. \(2013\)](#) method, approximately 2% higher than the [Aqrabi et al. \(2011\)](#), [Amin et al. \(2015\)](#), and [Shafiq et al. \(2015b\)](#) methods, and 1.5% higher than the [Amin and Deriche \(2015a\)](#) method. The results show the improved performance obtained using the proposed algorithm while keeping the algorithm complexity to the minimum.

#### Accuracy and complexity comparison of the proposed dictionary-based classifier

The proposed dictionary-based classifier detects salt domes with good accuracy. We compare the performance of the proposed dictionary-based classifier with the traditional Bayesian classifier discussed in [Berthelot et al. \(2012\)](#). We use the same set of attributes for both the classifiers. Figure 24 shows the classification accuracy for inlines #350–#359 in using the dictionary-based classifier and the Bayesian classifier. The dictionary-based classifier gives an average accuracy of 96.5%, which is 3.6% higher than the Bayesian classifier. However, the computational cost of the dictionary-based classifier is higher than the Bayesian classifier.

The proposed dictionary-based classifier solves the  $\ell_1$ -minimization problem to classify each patch. The sol-

**Table 4.** Precision, recall, and *F*-measure.

Salt-dome detection method	Precision	Recall	<i>F</i> -measure
Proposed method	98.97	94.24	96.55
<a href="#">Aqrabi et al. (2011)</a>	97.75	91.25	94.37
<a href="#">Berthelot et al. (2013)</a>	95.82	92.12	93.92
<a href="#">Amin and Deriche (2015a)</a>	97.93	92.63	95.21
<a href="#">Amin et al. (2015)</a>	98.84	90.08	94.26
<a href="#">Shafiq et al. (2015b)</a>	97.81	91.44	94.72

ution to the  $\ell_1$ -minimization is computationally expensive. General LP solvers are slow and therefore are not suitable for our application. In this work, we have used the homotopy-based solver (ul Haq et al., 2012) for the  $\ell_1$ -minimization problem. The accuracy of the homotopy-based solver is comparable with the general LP solvers, whereas the computational cost is significantly less. In Table 5, we show the computational complexity of the proposed dictionary-based classifier method using the homotopy method and the general LP solvers for five inlines. The running time for both approaches was computed using a core i-5 machine. The dictionary-based classifier using the homotopy method is three times computationally more efficient than the general LP solver-based method.

### **Classification accuracy with and without the proposed refining step**

As discussed in the previous section, we use a refining step based on the energy value and edge strength to estimate the boundary accurately within the classified patch. Without the proposed refining step, the boundary of the salt dome can be estimated by considering the bottom row pixels, middle row pixels, or the top row pixels of each patch as the boundary pixels. We com-

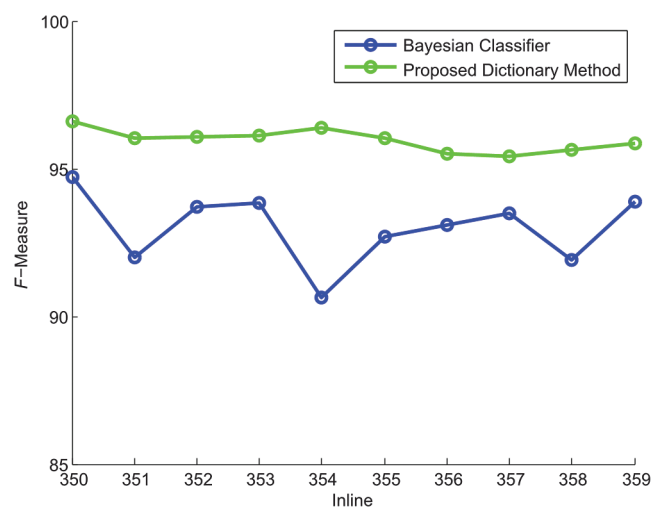


**Figure 24.** Dictionary-based classifier versus Bayes classifier (*F*-measure result).

**Table 5.** Time comparison: Homotopy versus general LP solver.

Inline #	Homotopy	General LP solver
350	28.3 s	74.24 s
351	31.75 s	80.28 s
352	29.52 s	77.52 s
353	30.93 s	79.62 s
354	28.84 s	74.87 s

**Table 6.** Accuracy comparison: Dictionary based classifier with and without refining.

Salt-dome detection method	<i>F</i> -measure
Proposed method (with refining)	96.55
Dictionary method (bottom pixels, without refining)	94.26
Dictionary method (middle pixels, without refining)	92.51
Dictionary method (top pixels, without refining)	91.79

pare the performance of the proposed refining step with the other three approaches in Table 6. We see that the refining step enhances the accuracy of the proposed algorithm. The dictionary-based method, using the proposed refining step, gives an average *F*-measure value of 96.55%, which is 2.5% higher than the dictionary-based method considering bottom pixels of patches as the boundary. The other two approaches give even lower *F*-measure values. The proposed refining step demonstrates a considerable enhancement as compared with no refining.

### **Conclusion**

In this paper, we introduced a new approach for salt-dome detection using a dictionary-based classification framework. The features used with such a framework consist of an optimal set obtained from the GLC matrix, Gabor filters, and higher order SVD, using an information theoretic feature ranking approach. We tested three popular feature ranking techniques, namely, the MIFS, mRMR, and JMI models. The JMI-based information theoretic model was shown to provide the best ranking methodology suitable for salt-dome detection. We also introduced a new boundary refining step for patch-based classification methods. This step was implemented using the energy values and the edge map computed for the classified patches. By combining the energy values and the edge map based refining step, together with the dictionary-based classification stage, we ensure that the proposed algorithm achieves excellent detection accuracy even when the salt boundary is represented by very weak reflectors. We tested our approach on the Netherlands offshore F3 block and showed that the proposed algorithm can detect salt bodies with excellent accuracy outperforming different existing techniques.

### **Acknowledgments**

This work is supported by the Center for Energy and Geo Processing (CeGP) at King Fahd University of Petroleum and Minerals (KFUPM) and Georgia Tech under Project no. GTEC 1401-1402.

### **References**

- Amin, A., and M. Deriche, 2015a, A hybrid approach for salt dome detection in 2D and 3D seismic data: IEEE Inter-

- national Conference on Image Processing (ICIP), IEEE, 2537–2541.
- Amin, A., and M. Deriche, 2015b, A new approach for salt dome detection using a 3D multidirectional edge detector: *Applied Geophysics*, **12**, 334–342, doi: [10.11007/s11770-015-0512-2](https://doi.org/10.11007/s11770-015-0512-2).
- Amin, A., and M. Deriche, 2016, Salt-dome detection using a codebook-based learning model: *IEEE Geoscience and Remote Sensing Letters*, **13**, 1636–1640, doi: [10.1109/LGRS.2016.2599435](https://doi.org/10.1109/LGRS.2016.2599435).
- Amin, A., M. Deriche, T. Hegazy, Z. Wang, and G. AlRegib, 2015, A novel approach for salt dome detection using a dictionary-based classifier: 85th Annual International Meeting, SEG, Expanded Abstracts, 1816–1820.
- Aqrabi, A. A., T. H. Boe, and S. Barros, 2011, Detecting salt domes using a dip guided 3D sobel seismic attribute: 81st Annual International Meeting, SEG, Expanded Abstracts, 1014–1018.
- Battiti, R., 1994, Using mutual information for selecting features in supervised neural net learning: *IEEE Transactions on Neural Networks*, **5**, 537–550, doi: [10.1109/72.298224](https://doi.org/10.1109/72.298224).
- Berthelot, A., A. H. Solberg, and L.-J. Gelius, 2013, Texture attributes for detection of salt: *Journal of Applied Geophysics*, **88**, 52–69, doi: [10.1016/j.jappgeo.2012.09.006](https://doi.org/10.1016/j.jappgeo.2012.09.006).
- Berthelot, A., A. H. S. Solberg, E. Morisbak, and L.-J. Gelius, 2012, 3D segmentation of salt using texture attributes: 82nd Annual International Meeting, SEG, Expanded Abstracts, doi: [10.1190/segam2012-1443.1](https://doi.org/10.1190/segam2012-1443.1).
- Brown, G., A. Pocock, M.-J. Zhao, and M. Luján, 2012, Conditional likelihood maximization: A unifying framework for information theoretic feature selection: *The Journal of Machine Learning Research*, **13**, 27–66.
- Donoho, D. L., Y. Tsaig, I. Drori, and J. Luc Starck, 2012, Sparse solution of underdetermined linear equations by stagewise orthogonal matching pursuit: *IEEE Transactions on Information Theory*, **58**, 1094–1121, doi: [10.1109/TIT.2011.2173241](https://doi.org/10.1109/TIT.2011.2173241).
- Gao, D., 2003, Volume texture extraction for 3D seismic visualization and interpretation: *Geophysics*, **68**, 1294–1302, doi: [10.1190/1.1598122](https://doi.org/10.1190/1.1598122).
- Haralick, R. M., K. S. Shanmugam, and I. Dinstein, 1973, Textural features for image classification: *IEEE Transactions on Systems, Man, and Cybernetics*, **SMC-3**, 610–621, doi: [10.1109/TSMC.1973.4309314](https://doi.org/10.1109/TSMC.1973.4309314).
- Hauks, J., O. R. Ravndal, B. Fotland, A. Bounaim, and L. Sonneland, 2013, Automated salt body extraction from seismic data using the level set method: *First Break*, **31**, P35–P42.
- Hegazy, T., and G. AlRegib, 2014, Texture attributes for detecting salt bodies in seismic data: 84th Annual International Meeting, SEG, Expanded Abstracts, 1455–1459.
- Jain, A. K., and F. Farrokhnia, 1991, Unsupervised texture segmentation using Gabor filters: *Pattern Recognition*, **24**, 1167–1186, doi: [10.1016/0031-3203\(91\)90143-S](https://doi.org/10.1016/0031-3203(91)90143-S).
- Jing, Z., Z. Yanqing, C. Zhigang, and L. Jianhua, 2007, Detecting boundary of salt dome in seismic data with edge-detection technique: 77th Annual International Meeting, SEG, Expanded Abstracts, 1392–1396.
- Lomask, J., and B. Biondi, 2003, Image segmentation for tracking salt boundaries: Stanford Exploration Project report, 193200.
- Lomask, J., B. Biondi, and J. Shragge, 2004, Image segmentation for tracking salt boundaries: 74th Annual International Meeting, SEG, Expanded Abstracts, 2443–2446.
- Lomask, J., R. G. Clapp, and B. Biondi, 2006, Parallel implementation of image segmentation for tracking 3D salt boundaries: 68th Conference and Exhibition, EAGE, Extended Abstracts, doi: [10.3997/2214-4609.201402339](https://doi.org/10.3997/2214-4609.201402339).
- Meyer, P. E., C. Schretter, and G. Bontempi, 2008, Information-theoretic feature selection in microarray data using variable complementarity: *IEEE Journal of Selected Topics in Signal Processing*, **2**, 261–274, doi: [10.1109/JSTSP.2008.923858](https://doi.org/10.1109/JSTSP.2008.923858).
- Peng, H., F. Long, and C. Ding, 2005, Feature selection based on mutual information criteria of max-dependency, max-relevance, and min-redundancy: *IEEE Transactions on Pattern Analysis and Machine Intelligence*, **27**, 1226–1238, doi: [10.1109/TPAMI.2005.159](https://doi.org/10.1109/TPAMI.2005.159).
- Randen, T., and L. Sønneland, 2005, *Atlas of 3D seismic attributes*: Springer.
- Shafiq, M. A., Z. Wang, and G. AlRegib, 2015a, Seismic interpretation of migrated data using edge-based geodesic active contours: Presented at the 2014 IEEE Global Conference on Signal and Information Processing (GlobalSIP), IEEE.
- Shafiq, M. A., Z. Wang, A. Amin, T. Hegazy, M. Deriche, and G. AlRegib, 2015b, Detection of salt-dome boundary surfaces in migrated seismic volumes using gradient of textures: 85th Annual International Meeting, SEG, Expanded Abstracts, 1811–1815.
- Shi, J., and J. Malik, 2000, Normalized cuts and image segmentation: *IEEE Transactions on Pattern Analysis and Machine Intelligence*, **22**, 888–905.
- ul Haq, Q. S., L. Tao, F. Sun, and S. Yang, 2012, A fast and robust sparse approach for hyperspectral data classification using a few labeled samples: *IEEE Transactions on Geoscience and Remote Sensing*, **50**, 2287–2302, doi: [10.1109/TGRS.2011.2172617](https://doi.org/10.1109/TGRS.2011.2172617).
- Wang, Z., T. Hegazy, Z. Long, and G. AlRegib, 2015, Noise-robust detection and tracking of salt domes in postmigrated volumes using texture, tensors, and subspace learning: *Geophysics*, **80**, no. 6, WD101–WD116, doi: [10.1190/geo2015-0116.1](https://doi.org/10.1190/geo2015-0116.1).
- Yang, H. H., and J. E. Moody, 1999, Data visualization and feature selection: New algorithms for non-Gaussian data: *NIPS*, Citeseer, 687–693.
- Zhang, Y., and A. Halpert, 2012, Enhanced interpreter-aided salt boundary extraction using shape deformation: 82nd Annual International Meeting, SEG, Expanded Abstracts, doi: [10.1190/segam2012-1337.1](https://doi.org/10.1190/segam2012-1337.1).



**Asjad Amin** received a B.S. (2007) in telecommunication engineering from the National University of Computer & Emerging Sciences NUFAST, Islamabad, Pakistan, and an M.S. (2012) in electrical engineering from the University of Engineering & Technology, Taxila, Pakistan. Since 2012, he has been with the Department of Electrical

Engineering at King Fahd University of Petroleum & Minerals, Saudi Arabia, where he completed a Ph.D. in 2016. He joined the Islamia University of Bahawalpur, Pakistan, as a lecturer in 2008. His research interests include image and video processing, seismic imaging and modeling, machine learning, and image segmentation.



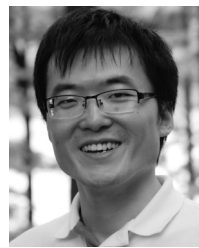
**Mohamed Deriche** received a Ph.D. (1993) from the University of Minnesota. He then joined the Queensland University of Technology, Australia, in 1994 where he led the Speech and Audio Research Lab. In 2001, he joined the EE Department at King Fahd University of Petroleum & Minerals, where he is leading the Signal Processing

Group. He has published more than 200 papers in multimedia signal and image processing. He has delivered numerous invited and tutorial talks. He has chaired several conferences including TENCON, GLOBALSIP-MPSP, IEEE GCC, and IPTA. He has supervised more than 35 M.S. and Ph.D. students. He has received the IEEE third Millennium Medal, the Shauman award for best researcher in the Arab World, and the Excellence in Research and the Excellence in Teaching awards at KFUPM, as well as several other awards. His research interests include multimedia signal and image processing, quality of experience, seismic data analysis, biometrics, and biomedical applications.



**Muhammad Amir Shafiq** received a B.S. (2006) in electrical engineering from the University of Engineering and Technology, Taxila, Pakistan. At Ghulam Ishaq Khan Institute of Engineering Sciences and Technology, Topi, he received an M.S. (2008) in electronics engineering. His work at National Engineering and Scientific Commission was

related to signal processing, embedded systems, and real-time implementation. Since 2008, he has written regularly in international journals and presented at conferences. As a student member of SEG, AAPG, EAGE, IEEE, and IEEE Signal Processing Society (SPS), he has been the reviewer of several international journals and conferences. He is a Fulbright Ph.D. scholar in the school of Electrical and Computer Engineering at the Georgia Institute of Technology, Atlanta, Georgia. He is working under the supervision of G. AlRegib in the CeGP. His research area is signal and image processing with a particular focus on seismic processing and interpretation. His research interests include digital signal and image processing, embedded systems, adaptive control, seismic interpretation, and geoprocessing.



**Zhen Wang** received a B.S. (2010) and an M.S. (2012) from the Shanghai Jiao Tong University, Shanghai, China. He received a second master's degree in electrical and computer engineering from Georgia Tech, USA, in 2012, where he is pursuing a doctoral degree. As a Ph.D. student of G. AlRegib, he is an active member in the Multimedia and Sensors Lab (MSL) and CeGP. He received the Wallace H. Coulter fellowship in 2010, a Samsung scholarship in 2011, and a Leo Koguan scholarship in 2012. As a student member of SEG, IEEE, and IEEE SPS, he has been a reviewer of international journals and conferences. His research interests include seismic interpretation, image and video processing, and computer vision.



**Ghassan AlRegib** is a professor in the School of Electrical and Computer Engineering at the Georgia Institute of Technology. He is the director of the MSL at Georgia Tech. In 2012, he was named the director of Georgia Tech's CeGP. He is a faculty member of the Center for Signal and Information Processing (CSIP). He also serves as the director of Georgia Tech's Initiatives and Programs in MENA. He has authored and coauthored more than 150 papers in international journals and conference proceedings. He has been issued five U.S. patents, two U.S. patent applications, and several invention disclosures. He is a senior member of IEEE. He received the ECE Outstanding Graduate Teaching Award in 2001 and the CSIP Research and the CSIP Service Awards in 2003. In 2008, he received the ECE Outstanding Junior Faculty Member Award. He serves as an area chair, ICME 2016, the tutorial chair, ICIP 2016. He is a member of the IEEE SPS Technical Committees on Multimedia Signal Processing and Image, Video, and Multidimensional Signal Processing, a member of the editorial board of the *Wireless Networks Journal* (WiNET), 2009–present, the IEEE Transaction on Circuits and Systems for Video Technology, 2014–present, and the Elsevier Journal *Signal Processing: Image Communications*, 2015–present. He served as the chair of the Special Sessions Program at ICIP'06, the area editor for Columns and Forums in the IEEE Signal Processing Magazine (SPM), 2009–2012, the associate editor for IEEE SPM, 2007–2009, the tutorials cochair in ICIP2009, a guest editor for IEEE J-STSP, 2012, a track chair in ICME2011, the co-chair of the IEEE MMTC Interest Group on 3D Rendering, Processing, and Communications, 2010–2012, the chair of the Speech and Video Processing Track at Asilomar 2012, and the Technical Program cochair of IEEE GlobalSIP, 2014. His research group of more than 20 students and researchers is working on projects related to image and video processing and communications, seismic imaging, perception in visual data processing, healthcare intelligence, and video analysis.